Aerosol remote sensing over the ocean using MSG-SEVIRI visible images

Y Bennouna, G de Leeuw, Jacques Piazzola, J Kusmierczyk-Michulec

Aerosol remote sensing over the ocean using MSG-SEVIRI visible images

Y. S. Bennouna,[1,2,3] G. de Leeuw,[1,4,5,6] J. Piazzola,[2] and J. Kusmierczyk-Michulec[1]

Received 11 December 2008; revised 10 June 2009; accepted 24 August 2009; published 11 December 2009.

[1] With its observational frequency of 15 minutes, the Meteosat Second Generation (MSG) geostationary satellite offers a great potential to monitor aerosol transport using Spinning Enhanced Visible and Infra-Red Imager (SEVIRI) data. To explore this potential, an algorithm for the retrieval of aerosol optical properties has been developed for use over the ocean. It is a multispectral algorithm based on the single-view algorithm for the Along Track Scanning Radiometer (ATSR-2) (Veefkind and de Leeuw, 1998) which has been adapted to the corresponding channels of SEVIRI (635 nm, 810 nm and 1640 nm). The SEVIRI Aerosol Retrieval Algorithm (SARA) provides the Aerosol Optical Depth (AOD) for these channels. To illustrate its capabilities, the application of this algorithm to two cases is presented: (1) a forest-fire smoke plume advected from Spain and Portugal over the Atlantic Ocean in August 2006, and (2) an outbreak of Saharan dust over the Western Mediterranean Sea in February 2006. The results obtained are validated with AERONET ground-based measurements for two coastal stations, and compared with the retrievals from the Moderate Resolution Imaging Spectroradiometer (MODIS) on NASA's Terra and Aqua satellites. The diurnal variations of the aerosol optical depth observed at the AERONET sites are well reproduced, and the spatial patterns retrieved using the SARA algorithm are in reasonable agreement with those observed by MODIS.

Citation: Bennouna, Y. S., G. de Leeuw, J. Piazzola, and J. Kusmierczyk-Michulec (2009), Aerosol remote sensing over the ocean using MSG-SEVIRI visible images, *J. Geophys. Res.*, *114*, D23203, doi:10.1029/2008JD011615.

1. Introduction

[2] Urbanization and industrialization have largely contributed to the increase of aerosol concentrations and to the change of the chemical composition of the lower troposphere. By absorbing and scattering the incoming solar radiation, atmospheric particles affect the amount of radiation reaching the surface, and therefore influence directly the earth radiative balance. Since they can act as condensation nuclei (hygroscopic particles with submicrometer sizes) or as ice nuclei (e.g., dust particles), they also influence indirectly the earth radiative balance by playing a key role in the formation of clouds. Aerosol-induced changes in the cloud microphysics can modify the cloud albedo [*Twomey*, 1977; *Twomey et al.*, 1984], influence cloud lifetime and precipitation [*Flossmann*, 1998]. Most aerosols have short lifetimes (days to weeks) and their properties change due to physical and chemical transformations in the atmosphere. Therefore, the geographical distribution of their physical, chemical and optical properties is highly variable both in time and space. Because of the complexity and variability of atmospheric aerosol processes, the role of aerosols remains one of the largest uncertainties in climate assessment [*Intergovernmental Panel on Climate Change* (*IPCC*), 2008]. To document the variability of aerosol properties, satellites provide a unique opportunity with an almost instantaneous view over a large spatial area using the same instrument and technique. The significance of the aerosol impact on climate as estimated from satellites is described by *Kaufman et al.* [2002].

[3] During the past decade, significant progress has been achieved in passive-remote-sensing of aerosols using space-based observations. In 1981, AVHRR (Advanced Very High Resolution Radiometer) provided the first aerosol information from space over oceans [*Griggs*, 1981]. Since then, a number of space-based instruments has emerged. Aerosol information has been derived from non-dedicated instruments such as ATSR (Along Track Scanning Radiometer) [*Veefkind*, 1999], TOMS (Total Ozone Monitoring Spectrometer) [*Torres et al.*, 2002], SeaWiFS (Sea-viewing Wide Field-of-view Sensor) [*von Hoyningen-Huene et al.*, 2003], and GOME (Global Ozone Monitoring Experiment) [*Kuśmierczyk-Michulec and de Leeuw*, 2005]. The new generation of dedicated sensors present narrow bands, multispectral and multidirectional characteristics, and several algorithms have been proposed

[1]TNO Defence, Security and Safety, The Hague, Netherlands.
[2]LEPI-LSEET, University of Toulon-Var, La Valette du Var, France.
[3]Atmospheric Optics Group, University of Valladolid, Valladolid, Spain.
[4]TNO B&O, Utrecht, Netherlands.
[5]Climate Change Unit, Finnish Meteorological Institute, Helsinki, Finland.
[6]Department of Physics, University of Helsinki, Helsinki, Finland.

0148-0227/09/2008JD011615

for application over both ocean and land cloud-free scenes: the POLDER (POLarization and Directionality of Earth Reflectance) algorithm [*Deuzé et al.*, 1999, 2001], the MODIS (Moderate Resolution Imaging Spectroradiometer) algorithm [*Tanré et al.*, 1997; *Kaufman et al.*, 1997; *Levy et al.*, 2007], the MISR (Multi-angle Imaging SpectroRadiometer) algorithm [*Martonchik et al.*, 1998, 2002], and the BAER (Bremen AErosol Retrieval) algorithm for MERIS (Medium-Resolution Imaging Spectrometer) [*von Hoyningen-Huene et al.*, 2006].

[4] The most difficult task in these algorithms is to separate the surface and atmospheric contributions to the top of the atmosphere (TOA) radiance, and this task becomes particularly challenging over "bright land surfaces" as opposed to "dark ocean surfaces". When surface correction has been achieved, or the surface contribution to the TOA reflectance has been eliminated, the path radiance remains. The path radiance contains the information on the aerosol in the atmospheric column, and to retrieve this information, aerosol models are used with an assumption of the most likely aerosol type in the region, based on a climatology or other a priori information. Most retrievals use algorithms which determine the best fit between the radiation measured at TOA, and that calculated using a Radiative Transfer Model (RTM) for one or several aerosol models. When available, the use of polarization in combination with radiance measurements is expected to reduce the dependency on the aerosol a priori, and to improve the quality of the retrievals [*Mishchenko et al.*, 1997]. The active Cloud-Aerosol Lidar with Orthogonal Polarization (CALIOP) onboard CALIPSO (Cloud-Aerosol Lidar and Infrared Pathfinder Satellite Observation) enhances the current capabilities in space-based aerosol observation, by delivering information on the vertical distribution of aerosols during both day and night [*Winker et al.*, 2003].

[5] However, for Low Earth Orbiting (LEO) satellites, the revisit time is at best one day. In contrast, the high temporal sampling of sensors carried onboard Geostationary Orbiting (GEO) satellites such as MSG-SEVIRI, providing high-frequency observations (every 15 minutes), allows a detailed description of the spatio-temporal characterization of aerosols which in turn could provide crucial information for aerosol-climate and transport studies. The solar radiation reflected within the three spectral bands of SEVIRI centered at 635, 810 and 1640 nm (the SEVIRI solar channels), is sensitive to all major aerosol types. Algorithms for the retrieval of aerosol properties from SEVIRI data were presented by *Brindley and Ignatov* [2006] and *De Paepe et al.* [2008]. The algorithm by *Brindley and Ignatov* [2006] is based on AVHRR, and *De Paepe et al.* [2008] extends this algorithm with an improved cloud mask. In this work we present an algorithm to retrieve aerosol information from SEVIRI data has been developed based on the single-view algorithm that was developed for Along Track Scanning Radiometer (ATSR-2) data over ocean [*Veefkind and de Leeuw*, 1998]. The methodology and the improvements developed for the SEVIRI Aerosol Retrieval Algorithm (SARA) to retrieve the Aerosol Optical Depth (AOD) and the Angstrom coefficient over ocean are presented in this paper. Before the retrieval step starts, the scene is screened for the presence of clouds using the methods described by *Bennouna et al.* [2009]. The methodology of the retrievals relies on the interpolation of reflectance and transmittance data for predefined aerosol types with monomodal particle size distributions, and for a range of sun-sensor geometries. This information is stored in look-up tables (LUTs) to speed up the retrieval process. To represent different aerosol components of both natural and anthropogenic origin, several new LUTs were created based on different database of the literature. These LUTs were generated with the Doubling and Adding radiative transfer model developed by KNMI (DAK) [*Stammes*, 2001]. To investigate the impact of particle shape on the retrievals, LUTs for dust aerosol types were created, for both spherical particles and for spheroidal particles [*Mishchenko et al.*, 1997]. In SARA, the reflectance of the sea surface is parameterized as a function of wind speed and chlorophyll concentration. The chlorophyll concentration values are taken from the monthly binned products of SeaWiFS. The aerosol mixture (fine and coarse) that minimizes the difference between pre-calculated and measured TOA reflectance is selected by a least square fitting procedure.

[6] SARA has been applied to two cases: (1) a smoke plume due to forest fires in Spain and Portugal and transported over the Atlantic Ocean, and (2) a Saharan dust outbreak over the eastern Mediterranean Sea. The results were evaluated against time series from Sun photometer measurements at two AERONET sites located on the coast, showing that diurnal variations are well reproduced. Spatial trends were evaluated by comparison of the AOD retrieved from SEVIRI radiances and the MODIS aerosol product, for two different time slots acquired during the aforementioned events.

2. Algorithm Description

2.1. MSG-SEVIRI Radiance Data

[7] METEOSAT-8, launched in August 2002, is the first of a new generation of highly advanced weather satellites within the Meteosat Second Generation (MSG) program of EUMETSAT [*Schmetz et al.*, 2002]. MSG is a spin stabilized satellite orbiting geosynchronously at about 36000 km above the earth surface. The SEVIRI instrument onboard the MSG satellite delivers a full scan of the earth disk centered over the Equator and the 0 longitude every 15 minutes. This radiometer measures simultaneously the radiance in 11 narrow spectral bands: 3 solar channels (0.6, 0.8 and 1.6 μm), 8 infrared channels, and in one broad band 0.3–0.7 μm. SEVIRI provides images at a resolution of 3 km at the subsatellite point for the 11 narrow bands, and at a higher resolution of 1 km for the broad band channel. In this study, MSG-SEVIRI data were provided by KNMI in numerical counts which have been converted to radiances using the calibration coefficients as provided by EUMETSAT. Since aerosol information is mostly contained in measurements at the shortest wavelengths (i.e. VIS and near-infrared), SARA uses the SEVIRI data for two visible wavelengths, 635 nm and 810 nm, and one near-infrared wavelength: 1.64 μm.

2.2. Cloud Mask

[8] The retrieval of aerosol properties is possible only for cloud-free scenes. This requires rigorous cloud screening for which a fast and stand-alone algorithm has been imple-

Table 1. Size Distribution Parameters and Microphysical Properties for the Aerosol Models Used to Generate the Different LUTs

			$m(\lambda) = n + ik$		
LUT Label	$R_g(\mu m)$	σ_g	635 nm	810 nm	1640 nm
NAMb1	0.03	2.03	1.37 + i0.00002	1.37 + i0.00004	1.36 + i0.00050
NAMsoc	0.24	2.03	1.39 + i0.00000	1.38 + i0.00000	1.37 + i0.00030
OPACwaso	0.03	2.24	1.40 + i0.00212	1.39 + i0.00327	1.37 + i0.00633
OPACssam	0.42	2.03	1.35 + i0.00000	1.35 + i0.00000	1.33 + i0.00015
OPACmiam	0.39	2.00	1.53 + i0.00450	1.53 + i0.00400	1.53 + i0.00609
OPACmitr	0.50	2.20	1.53 + i0.00450	1.53 + i0.00400	1.53 + i0.00609
MODISc8	0.60	1.82	1.53 + i0.00000	1.53 + i0.00000	1.46 + i0.00100
MODISc9	0.50	2.22	1.53 + i0.00000	1.53 + i0.00000	1.37 + i0.00100

mented [*Bennouna et al.*, 2009]. The method used to identify cloud contaminated pixels is based on the work of *Saunders and Kriebel* [1988]. The main structure of the routines implemented for SEVIRI is similar to the automated version implemented by *Robles-Gonzalez* [2003] for ATSR-2 which in turn is based on the algorithm developed by *Koelemeijer et al.* [2001]. The code was adapted to fit the characteristics of MSG-SEVIRI, and updated according to the improvements implemented in the APOLLO cloud analysis tool [*Kriebel et al.*, 2003]. The dynamic thresholding technique adopted in the TNO stand-alone Cloud Detection Algorithm (TNO-CDA) is based on image histogram analysis which makes use of a limited number of spectral data: the reflectance in two visible channels of SEVIRI ($R_{0.6}$, $R_{0.8}$), and the brightness temperature in the thermal infrared channels at 10.8 μm and 12 μm ($T_{10.8}$, T_{12}). The detection process is based on a test sequence involving 4 different tests (with different test sequences for land and ocean pixels): the Infrared Gross Temperature Test (test 1), the Spatial Coherence Test (test 2), the Dynamic Visible Test (test 3) and the Dynamic Ratio Test (test 4). The Infrared Gross Temperature Test uses the 12.0 μm brightness temperature data to detect the coldest areas in the image ($T_{12} < T_{12}^{lim}$), which indicate the presence of medium or high clouds. The Spatial Coherence Test is used exclusively over the ocean. The largest standard deviations (STD) of the 10.8 μm brightness temperature in a 3 × 3 pixel array ($STD_{10.8} > STD_{10.8}^{lim}$), allow to detect small cloud amounts and clouds presenting low optical thickness (i.e. cloud edges, thin cirrus, and small cumulus). The Dynamic Visible Test (test 3) takes advantage of the strong reflectance of clouds as compared to that of land and sea surfaces ($R_{0.6} > R_{0.6}^{lim}$ over land, $R_{0.8} > R_{0.8}^{lim}$ over sea). This test principally detects low cloud targets. The Dynamic Ratio Test uses the value of the reflectance ratio ($R_{0.8}/R_{0.6}$) to discriminate between cloud contaminated ($R_{0.8}/R_{0.6} \sim 1$), land ($R_{0.8}/R_{0.6} > 1$) and sea($R_{0.8}/R_{0.6} < 1$) pixels. The suitable temperature, reflectance and reflectance ratio thresholds, are determined by analyzing the numerically calculated extreme points of the smoothed histogram data. The detailed description of this cloud screening technique, and its evaluation over Western Europe, is reported by *Bennouna et al.* [2009].

2.3. LUTs

2.3.1. Aerosol Models

[9] Optical properties of aerosols are determined by their size distribution and their chemical composition which is related to the refractive index. In this study, 3 sets of LUTs have been created. Each of these sets is based on various sources of information including the Navy Oceanic Vertical Aerosol Model [*de Leeuw et al.*, 1989], the Optical Properties of Aerosols and Clouds (OPAC) database [*Hess et al.*, 1998], and the MODIS aerosol retrieval algorithm [*Remer et al.*, 2006]. The different size distribution parameters and refractive indices used to build the different LUTs are listed in Table 1. Unlike dust, sea salt and water soluble aerosols are hygroscopic particles. Here, the mean geometric radius and the refractive indices have been determined at 80% relative humidity [*Shettle and Fenn*, 1979]. Two different models of sea salt and water soluble aerosols have been tested: the types labeled as 'NAMb1' and 'NAMsoc' are defined from the NOVAM model, 'OPACwaso' and 'OPACssam' are based on the OPAC database. For dust particles, the mineral accumulation mode ('OPACmiam') and the mineral transported model ('OPACmitr') from OPAC were used, as well as the 2 dust aerosol types proposed in the MODIS aerosol retrieval algorithm ('MODISc8' and 'MODISc9'). For each aerosol type the parameters r_g (mean geometric radius) and σ_g (geometric standard deviation) define the distribution of the normalized number concentration n, represented by a monomodal lognormal function of the particle radius r [*Seinfeld and Pandis*, 1998]:

$$n(r) = \frac{dn}{dr} = \frac{1}{r \cdot \sqrt{2\pi} \cdot \ln \sigma_g} \exp \frac{-\left(\ln r - \ln \bar{r}_g\right)^2}{2 \cdot \ln^2 \sigma_g} \qquad (1)$$

In most climate and radiative transfer models, optical properties of aerosols are modeled assuming particle sphericity. This assumption is based on the simple physical principle that liquid aerosols have a spherical shape because of surface tension. However, soot agglomerate and dust aerosols are non-hygroscopic solid aerosols which are typically irregularly shaped [*DeCarlo et al.*, 2004; *Kalashnikova and Sokolik*, 2002]. The nonsphericity aspect of dust particles can have a significant impact on their optical properties in the solar spectrum [*Yang et al.*, 2007]. Spheroid models can closely reproduce light scattering matrices obtained from laboratory measurements of desert dust particles [*Volten et al.*, 2001]. In this study, the scattering matrices of spherical particles are calculated with the code developed by *de Rooij and van der Stap* [1984] based on the Lorentz-Mie theory [*Mie*, 1908; *van de Hulst*, 1957; *Kerker*, 1969]. The impact of particle shape on the retrievals has been investigated with the T-Matrix code [*Mishchenko and Travis*, 1994] which rigorously computes light scattering by randomly oriented spheroid particles. For

Table 2. Spectral Single Scattering Albedo and Asymmetry Parameter for the Different Aerosol Types and Wavelengths of SEVIRI

	$\omega_0(\lambda)$			$g(\lambda)$		
LUT Label	635 nm	810 nm	1640 nm	635 nm	810 nm	1640 nm
NAMb1	0.9997	0.9994	0.9811	0.6257	0.5759	0.3946
NAMsoc	1.0000	1.0000	0.9976	0.7620	0.7660	0.7627
OPACwaso	0.9828	0.9708	0.9004	0.6918	0.6680	0.5608
OPACssam	1.0000	1.0000	0.9984	0.7844	0.7892	0.8050
OPACmiam	0.9080	0.9330	0.9471	0.7170	0.6999	0.6875
OPACmitr	0.8589	0.8926	0.9148	0.7622	0.7383	0.7041
MODISc8	1.0000	1.0000	0.9901	0.6988	0.6824	0.7203
MODISc8 (nonspherical)	0.9999	0.9999	0.9951	0.6255	0.6770	0.7420
MODISc9	1.0000	1.0000	0.9833	0.7242	0.7096	0.7225
MODISc9 (nonspherical)	0.9999	0.9999	0.9948	0.6627	0.7116	0.7050

both spherical and nonspherical models, the values of the single scattering albedo w_0 and asymmetry parameter of the phase function g are presented in Table 2.

2.3.2. Radiative Transfer Simulations

[10] To model the TOA reflectance measured by SEVIRI, the algorithm uses pre-calculated LUTs which provide the modeled bidirectional reflectance/transmittance data, and transmission functions for a pre-defined atmosphere in the three channels 635, 810 and 1640 nm. Each LUT corresponds to a different type of aerosol (i.e. size distribution parameters and chemical composition), except the 'Rayleigh LUT' which represents the case of a purely molecular atmosphere, without aerosols. Various sets of aerosol models were used to build the LUTs dedicated to MSG-SEVIRI retrievals. The different aerosol types are described in section 2.3.1. Reflectance, transmittance, and transmission quantities which are stored in the LUTs are computed using the KNMI Doubling and Adding radiative transfer model (DAK) [*Stammes*, 2001]. DAK is developed for line-by-line or monochromatic multiple scattering calculations at UV, visible, and near-infrared wavelengths in a horizontally homogeneous atmosphere using the doubling adding method [*de Haan et al.*, 1987]. For the results presented in this paper, the atmospheric profile for pressure, temperature and humidity is based on the Midlatitude Summer (MLS) and the Midlatitude Winter (MLW) reference atmospheres [*McClatchey et al.*, 1972]. For all simulations, the aerosol layer was assumed to be 2 km high and concentrations decrease exponentially with altitude. The signal measured by the satellite is simulated for various scenarios, including multiple sun-satellite geometries and various aerosol loads: 15 solar and viewing zenith angles, 37 azimuth angles, and 11 optical depths at the reference wavelength of 500 nm (ranging between 0.02 and 6). All physical parameters available in the LUTs are listed and described in Table 3.

2.4. Reflectance Model Over Sea

2.4.1. Sea Surface Reflectance

[11] SARA accounts for the bidirectional reflectance of the ocean. The ocean reflectance is assumed to be the sum of specular reflection, reflection from oceanic whitecaps, and subsurface reflection [*Koepke*, 1984]. Given A_{wc}, the fraction of the ocean covered with whitecaps for a surface wind speed U in m.s^{-1} [*Monahan and Muircheartaigh*, 1980]:

$$A_{wc} = 3.84 \cdot 10^{-6} \cdot U^{3.41} \tag{2}$$

the total sea surface reflectance can be expressed as:

$$\rho_{sea} = \underbrace{(1 - A_{wc})\rho_g}_{(1)} + \underbrace{A_{wc} \cdot \rho_{wc}}_{(2)} + \underbrace{(1 - A_{wc}) \cdot \rho_u}_{(3)} \tag{3}$$

In equation 3 the sea surface reflectance is composed of one bidirectional component also called glint (1) and two isotropic components (equations (2) and (3)). The first term describes the specular reflectance (Fresnel reflection) at the water surface, which applies in the absence of whitecaps (cf. $(1 - A_{wc})$ for area not covered by whitecaps). When the ocean surface can be approximated by a flat surface, the specular reflectance is calculated using the classical Fresnel coefficient formula [*Fresnel*, 1827]. When the roughness effect is taken into account, the Fresnel reflection coefficient

Table 3. Variables Stored in the LUTs

Parameter	Symbol	Dependence	Dimension
Surface pressure	p		1
Wavelength	λ		3
Reference AOD at 500 nm	τ_{500}		11
Cosine of solar Zenith Angle	μ_s		15
Cosine of viewing Zenith Angle	μ_v		15
Relative Azimuth Angle	ϕ		37
Single Scattering Albedo	w_0	(λ)	3
Asymmetry Parameter	g	(λ)	3
Spectral AOD	τ	(λ, τ_{500})	(3, 11)
Bidirectional reflectance at the TOA	ρ_{atm}	$(\lambda, \tau_{500}, \mu_s, \mu_v, \phi)$	(3, 11, 15, 15, 37)
Bidirectional transmittance at the surface	T_{bd}	$(\lambda, \tau_{500}, \mu_s, \mu_v, \phi)$	(3, 11, 15, 15, 37)
Transmission function of the atmosphere	T_{tot}	$(\lambda, \tau_{500}, \mu_s, \mu_v)$	(3, 11, 15, 15)
Total downward transmission of the atmosphere	$T_{tot}^{\downarrow}$	$(\lambda, \tau_{500}, \mu_s)$	(3, 11, 15)
Total downward diffuse transmission of the atmosphere	$t^{\downarrow}$	$(\lambda, \tau_{500}, \mu_s)$	(3, 11, 15)

of a wavy sea surface can be calculated using a probability distribution function of surface wave slope [*Cox and Munk*, 1954]. Term (2) quantifies the reflectance due to the presence of whitecaps. The spectral values of the foam reflectance ρ_{wc} are based on the laboratory measurements performed by *Whitlock et al.* [1982]. In situ measurements of foam reflectance have been carried out by e.g., *Moore et al.* [2000]; *Kokhanovsky* [2004]. Term (3) represents the water leaving reflectance or underlight which is the reflectance caused by the water constituents below the ocean surface. The below- and above-water upwelling radiances and fluxes expressed by *Gordon and Morel* [1983] and *Morel and Gentili* [1996] lead to a relation which defines the water leaving reflectance by covering both effects of reflection and refraction at the air-sea interface [*Ruddick et al.*, 2006]:

$$\rho_u = \pi \cdot \frac{(1-\rho_w)\cdot(1-\overline{\rho}_w)}{n_w^2} \cdot \frac{R}{Q} \tag{4}$$

In this equation, the index w refers to pure sea water, $\rho_w(\sim 0.021)$ is the Fresnel reflectance for upwelling radiance from water to air, $\overline{\rho}_w(\sim 0.043)$ is the coefficient for downwelling flux from air to water, and n_w the refractive index of water ($\sim$1.33 in the visible and near infrared). R is the irradiance reflectance (or albedo) just beneath the sea surface, and Q relates the upwelling radiance to the irradiance just beneath the sea surface. *Gordon et al.* [1988] have shown that for case 1 water, the ratio $\frac{R}{Q}$ can be approximated by:

$$\frac{R}{Q} = 0.11 \cdot \frac{b_b}{K_d} \tag{5}$$

Thus the water leaving reflectance is related to its inherent optical properties, i.e. the total backscatter coefficient b_b and the diffuse attenuation coefficient K_d.

[12] *Morel and Prieur* [1977] have proposed a classification of sea water according to their constituents. For case 1 water, it was shown that water color mainly depends on phytoplankton concentrations. Therefore, the index usually adopted to specify the bio-optical state of case 1 water is its chlorophyll concentration [*Smith and Baker*, 1978]. Both the backscatter and diffuse attenuation coefficients can be expressed as the sum of specific coefficients related to pure sea water (b_{bw}, K_{dw}) and chlorophyll (b_{bc}, K_{dc}):

$$b_b = b_{bw} + b_{bc} \tag{6}$$

$$K_d = K_{dw} + K_{dc} \tag{7}$$

The values used for the coefficients of pure sea water are based on the measurements of *Smith and Baker* [1981]. ρ_u can be expressed as a function of the chlorophyll-a concentration *Chl*, using the bio-optical models formulated by *Morel* [1988] for the backscatter coefficient:

$$b_{bc}(\lambda) = 0.30 \cdot Chl^{0.62} \cdot \left(2.10^{-3} + 2.10^{-2} \cdot (0.50 - 0.25 \cdot \log Chl) \cdot \frac{0.550}{\lambda}\right) \tag{8}$$

and by *Baker and Smith* [1982] for the diffuse attenuation coefficient:

$$K_{dc}(\lambda) = k_c(\lambda) \cdot Chl \cdot \exp\left(-\left(k_c'(\lambda) \cdot \log(2 \cdot Chl)\right)^2\right) + 0.001 \cdot Chl^2 \tag{9}$$

In equation 9, k_c and k_c' are fitting parameters. Regarding the results presented in this paper, the surface wind speed has been fixed to a value of 5 m.s^{-1} for the whole area of study. The sea-surface chlorophyll concentration is extracted from the data of the SeaWiFS Level-3 monthly product for chlorophyll-a concentration [*Campbell et al.*, 1995].

2.4.2. TOA Reflectance

[13] By combining the bidirectional reflectance of the sea surface with atmospheric scattering, the total TOA reflectance over the ocean can be expressed as the sum of five terms corresponding to the different paths a photon might follow in the atmosphere [*Tanré et al.*, 1979]:

$$\rho = \underbrace{\rho_{atm}}_{(1)} + \underbrace{T^{\downarrow}\rho_{sea,dir}T^{\uparrow}}_{(2)} + \underbrace{t^{\downarrow}\rho_{sea,dif}T^{\uparrow}}_{(4)} + \underbrace{T^{\downarrow}\rho'_{sea,dif}t^{\uparrow}}_{(3)} + \underbrace{t^{\downarrow}\rho_{sea,iso}t^{\uparrow}}_{(5)} \tag{10}$$

All the above terms are functions of the wavelength and the sun-view geometry (i.e. sun and satellite zenith angles, and relative azimuth angle). The first term ρ_{atm} is called the path reflectance by aerosols and molecules (i.e., gases), which corresponds to the reflectance of the atmospheric layer containing both aerosol and gases as if there was no underlaying surface. T and t ($^{\uparrow}$ upward or $^{\downarrow}$ downward) stand for the direct and diffuse transmission of the atmosphere. Direct transmissions are assumed to be an exponential function of the aerosol optical depth τ:

$$T = \exp\left(\frac{-\tau}{\mu}\right) \tag{11}$$

where μ is either the cosine of the solar zenith angle (μ_s) for the direct transmission in the downward direction, or the cosine of the viewing angle (μ_v) for the direct transmission in the upward direction. The downward diffuse transmission is directly provided by the LUTs (cf. Table 3). The transmission downward (upward) is considered to be the sum of the diffuse and the direct transmissions downward (upward). The diffuse transmission in the upward direction can thus be derived from the LUTs data using:

$$t^{\uparrow} = \frac{T_{tot}}{(T^{\downarrow} + t^{\downarrow})} - T^{\uparrow} \tag{12}$$

In equation 10, terms (2), (3), (4) and (5) include the contributions of the specular reflection, oceanic whitecaps and underlight from the sea surface. $\rho_{sea,dir}$ is the Bidirectional Reflectance (BR) of the sea surface. $\rho_{sea,dif}$ is the hemispherical-directional reflectance of the sea surface (i.e. calculated using the convolution of the total irradiance with the surface BR function), and $\rho'_{sea,dif}$ is its equivalent in the reciprocal geometry. $\rho_{sea,iso}$ is the bihemispherical reflectance i.e. obtained from integration

of the BR function over all exiting angles under perfectly isotropic illumination. A wavy ocean, as described by *Cox and Munk* [1954], is assumed for the computation of the term related to the direct contribution (2), and a flat interface is assumed for the computation of the diffuse components (equations (3), (4), and (5)). As it was shown by *Takashima and Masuda* [1985], the latter approximation has very little effect on the retrievals.

2.5. Retrieval Method

[14] The method applied by SARA for ocean aerosol retrievals is similar to the single-view algorithm that was first developed for ATSR-2 [*Veefkind*, 1999; *Robles-Gonzalez*, 2003], and later applied to AATSR [*Curier et al.*, 2009]. This method is used to derive the AOD at the 3-km pixel level of SEVIRI (nadir resolution), in the three solar channels of the instrument. In the retrieval method, the first assumption relies on the separation of the TOA reflectance into the TOA reflectance of an atmosphere-ocean system in the absence of aerosols (ρ_0), and the reflectance caused by the presence of aerosols (ρ_{aer}):

$$\rho(\lambda) = \rho_0(\lambda) + \rho_{aer}(\lambda) \tag{13}$$

In the algorithm, an external mixture of two aerosol types is considered: one type represents the dominant aerosol type for the fine mode (anthropogenic/pollution), and the other the dominant aerosol type for the coarse mode (natural particles). In the same way as was done in the retrieval scheme of MODIS [*Remer et al.*, 2005], the effect of the multiple interactions among the different aerosol types is modeled with a standard linear mixing approach: the TOA reflectance for the mixture of two aerosols is approximated as a weighted average of the reflectances from the individual modes, as if they were alone in the atmosphere [*Wang and Gordon*, 1994]. If the fraction associated with the contribution of the fine mode to the TOA reflectance is called ν, the TOA reflectance can thus be expressed by:

$$\rho_{aer}(\lambda) = \nu \cdot \rho_f(\lambda) + (1-\nu) \cdot \rho_c(\lambda) \tag{14}$$

where ρ_f and ρ_c represent the reflectance due to the fine and the coarse mode respectively. With the help of equation 10 and the variables from the LUTs interpolated to the appropriate geometry, the TOA reflectance is calculated both for a purely molecular atmosphere (ρ_0^{lut}), and for an atmosphere composed of both aerosols and gases (ρ^{lut}). ρ^{lut} is determined for different fine/coarse aerosol mixtures, and for all tabulated values of the AOD at the reference wavelength of 500 nm. The best model is chosen by minimizing the least square error ϵ expressed as:

$$\epsilon_{\nu,f,c,\tau_{500}} = \sum_{i=1}^{n} \left(\frac{\rho^{meas}(\lambda_i) - \rho^{lut}(\lambda_i, \tau_{500})}{\rho^{meas}(\lambda_i) - \rho_0^{lut}(\lambda_i)} \right)^2 \tag{15}$$

This regression compares the sensor measurements ρ^{meas} in n selected channels of the instrument, with ρ^{lut}, the estimate of the TOA reflectance provided by the LUT data for the same wavelengths. For weakly absorbing aerosols and small optical depths [*Veefkind*, 1999; *Kokhanovsky et al.*, 2009] we can assume a linear relationship between the reflectance due to aerosols and the AOD [*Durkee et al.*, 1986]. Hence, if the AOD is noted as τ:

$$\rho_{aer}(\lambda) = C(\lambda) \cdot \tau(\lambda) \tag{16}$$

The spectral values of C depend on the aerosol type. The fine-coarse combination and the fraction ν that best fits the remote sensed data determine the model (i.e. spectral values of C) used to derive the AOD. Given the two aerosol types (fine and coarse) and ν for which $\epsilon_{\nu,f,c,\tau_{500}}$ is minimal, $C(\lambda)$ $C(\lambda)$ is estimated for each wavelength:

$$C(\lambda) = \frac{\rho_{aer}^{lut}}{\tau^{lut}} = \frac{\nu \cdot \rho_f^{lut}(\lambda, \tau_{500}) + (1-\nu) \cdot \rho_c^{lut}(\lambda, \tau_{500})}{\nu \cdot \tau_f^{lut}(\lambda, \tau_{500}) + (1-\nu) \cdot \tau_c^{lut}(\lambda, \tau_{500})} \tag{17}$$

and the spectral AOD can be derived as follows:

$$\tau^{meas}(\lambda) = \frac{\rho_{aer}^{meas}}{C(\lambda)} = \frac{\left(\rho^{meas}(\lambda) - \rho_0^{lut}(\lambda)\right)}{C(\lambda)} \tag{18}$$

In the SARA algorithm, the set of equations is solved for the first three bands of the MSG-SEVIRI instrument (i.e. 635, 810 and 1640 nm), and the fraction ν is chosen among 50 regularly spaced values between 0 and 1. For high AODs, the linear approximation mentioned in equation 16 cannot be used because the TOA reflectance plateaus for large AOD values. For this reason, if the best model corresponds to an AOD higher than 1, a third-order polynomial approximation is used to derive the AOD.

3. Sets for Data Evaluation

3.1. AERONET Data Set

[15] AERONET is an international network of automated Sun photomoters [*Holben et al.*, 1998] established by NASA. AERONET involves more than 300 automatically operating instruments worldwide. Standardization imposes sun and sky measurements of the downwelling radiation for a number of defined wave bands (340, 380, 440, 500, 675, 870, 1020 nm). The aerosol optical depth derived from these measurements is available from a free-access database. This database also provides other inversion products [*Dubovik and King*, 2000] characterizing aerosol optical, microphysical and radiative properties which are of great interest for aerosol research studies and satellite validation. In the current study, we used Level 1.5 (cloud-screened) and Level 2.0 (cloud-screened and quality-assured) data from two AERONET stations: Cabo da Roca (38N, 9W), and Forth Crete (35N, 25E).

3.2. MODIS Aerosol Product

[16] The polar-orbiting MODIS [*Salomonson et al.*, 1989] aboard Terra and Acqua spacecrafts acquires data for the entire Earth every 1 to 2 days. It measures the radiance in a large spectral range composed of 36 spectral bands between 0.405 and 14.385 μm, at three spatial resolutions of 250 m, 500 m, and 1000 m, with a wide swath of 2330 km. With such characteristics, this instrument was uniquely designed for monitoring ambient aerosols, clouds, and further allows the derivation of various products for remote sensing applications over land, ocean, and atmosphere. Aerosol

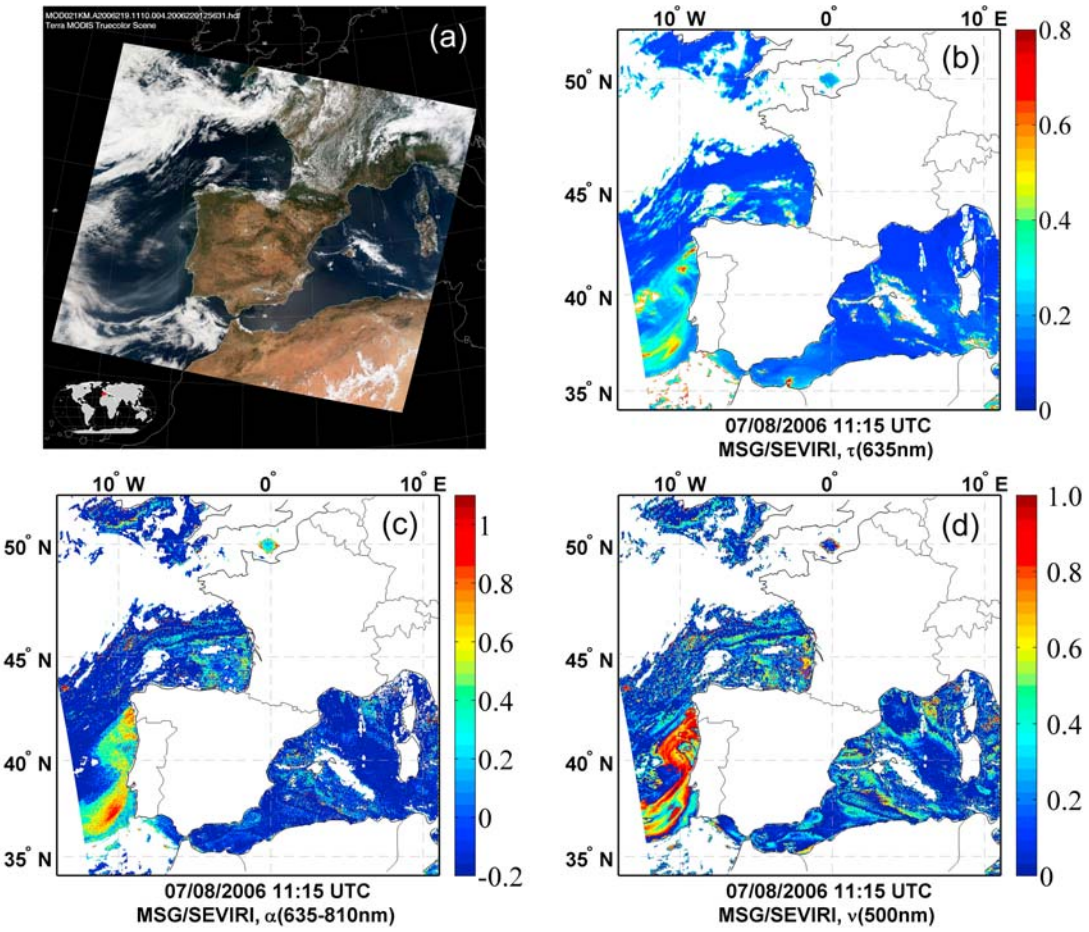

Figure 1. (a) True color image from the MODIS Terra/Aqua collection and (b, c, and d) results from SARA retrievals for the smoke plume from forest fires in Portugal advected over the Atlantic Ocean on 7 August 2006 at 11:15 UTC. Maps (resolution $\sim 5 \times 7$ km^2) show AOD at 635 nm (Figure 1b), Ångström coefficient 635–810 nm (Figure 1c), and weight of the fine/coarse mode aerosol on the AOD at 500 nm (Figure 1d).

properties are retrieved using two independent algorithms. The theoretical basis of the algorithms for application over land is described by *Kaufman et al.* [1997], and over ocean by *Tanré et al.* [1997]. Ocean and land retrievals have been validated by means of comparison with AERONET data [*Ichoku et al.*, 2002; *Chu et al.*, 2002; *Remer et al.*, 2002; *Levy et al.*, 2003, 2005]. The accuracy of the AOD retrievals over the ocean is: $\delta\tau = \pm 0.15\tau \pm 0.05$ as reported after revision of pre-launch estimation [*Remer et al.*, 2005]. The MODIS algorithm relies on a LUT approach. The MODIS algorithm models the ambient aerosol as a combination of one fine and one coarse mode following individual log-normal distributions. The measurement is compared to pre-calculated radiative transfer calculations for 9 aerosol types (4 'fine', and 5 'coarse'), and the inversion finds two solutions: the best and the average least square fit. In the Level-2 Atmosphere products of MODIS collection 5 [*Remer et al.*, 2006], both Terra and Aqua MODIS aerosol products (MOD04/MYD04-C005) provide global spectral AOD values over the ocean and the continents for cloud-free regions at 10 km resolution. These products also include the fractional contribution of the fine aerosol mode to the total AOD at 0.55 μm, and the type of aerosol identified by the retrieval. The SEVIRI channels in the visible and near-infrared are close to channels on Terra/Aqua MODIS. Therefore, aerosol retrievals derived from these two instruments can provide relevant comparisons to study the spatial variability of the AOD obtained with SARA.

4. Case Studies

[17] The applicability of the SARA algorithm for MSG-SEVIRI data over sea was tested for two case studies. The first event presented is the advection of strong forest-fire plumes from Portugal and Galicia (Spain) over the Atlantic Ocean. The second concerns a dust outbreak from the Saharan desert over the Western Mediterranean Sea. The values of the AOD and its diurnal variability are validated against AERONET measurements which are considered as 'ground truth'. In addition, the ability to reproduce the spatial variations is evaluated through comparisons with data from the MODIS aerosol product.

4.1. Transport of Forest Fire Smoke Over the Atlantic Ocean

[18] Large forest fires contribute to global warming in a "positive feedback loop": huge amounts of carbon dioxide

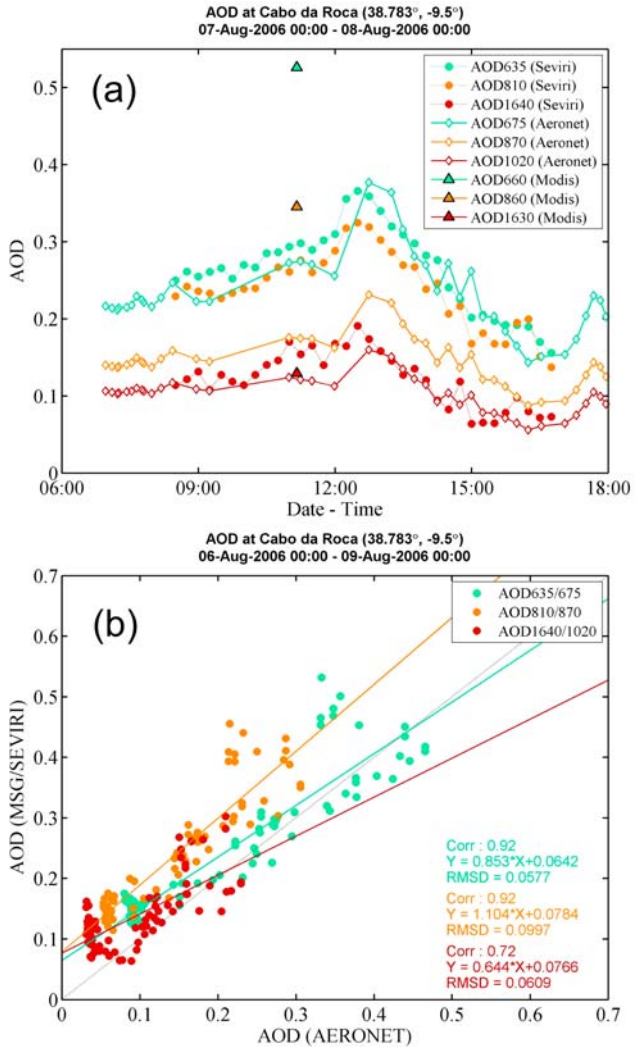

Figure 2. Comparison of the AOD retrieved using SARA with AERONET data at Cabo da Roca for the period 6–8 August 2006. (a) Time series (7 August 2006). (b) Scatterplots (6–8 August 2006). In Figure 2a the open diamonds stand for AERONET data, the dots represent SARA retrievals, and the triangles are the aerosol product for the MODIS overpass.

and other "planet-warming" greenhouse gases are released into the atmosphere, and global warming enhances the conditions that favors forest fires. In Europe, climate change seems to induce more frequent and longer heat waves of high intensity, with increasing likelihood of forest fires in the Mediterranean regions.

[19] In summer 2006, the Iberian peninsula experienced one of its most severe droughts. By August 7, many severe wildfires occurred across Galicia (Spain) and northern Portugal. Figure 1a shows the smoke plumes produced by forest fires which can be seen in the MODIS RGB picture (Terra) at 11:10 UTC.

4.1.1. SEVIRI Retrieval Results

[20] For the forest fire case, two separate aerosol retrievals were performed with SARA, each retrieval corresponding to a different set of aerosols, namely the 'OPAC' and the 'NAM' sets (see section 2.3.1). Thus, the retrievals done in the first simulation are constrained to use a mixture of 'NAMb1' (water soluble) and 'NAMsoc' (sea salt), and the retrievals done in the second simulation are constrained to use a mixture of 'OPACwaso' (water soluble) and 'OPACssam' (sea salt). Since the results obtained with the 'NAM' and the 'OPAC' models are very similar, only the 'OPAC' retrievals which give a slightly better agreement with AERONET, are presented here. The AOD retrieved from MSG-SEVIRI radiance data at 11:15 UTC is shown in Figure 1b. High values of the AOD located in the middle of the smoke plume contrast with the clean maritime background characterized by low AOD values (<0.1). The AOD at 635 nm retrieved with the SARA algorithm in the plume ranges mostly between 0.3 and 0.5, with maxima around 0.7. Outside the plume, high AOD values also appear near cloud edges. These are artifacts due to remaining cloud contamination.

[21] The Ångström coefficient was inferred from the retrieved AOD, using a band combination of the two SEVIRI visible channels, centered at 635 nm and 810 nm. The spatial variation of the Ångström coefficients is presented in Figure 1c. It shows that α has values in the plume of 0.6–1, whereas outside the plume they are around 0. This indicates the presence of small particles within the plume. Figure 1d shows that the high AOD observed over the plume is mostly due to the contribution of the fine mode, with values of ν mainly above 0.8.

4.1.2. Validation With AERONET

[22] To validate the results of SARA, the latter were compared to AOD measured at the AERONET site of Cabo da Roca (38N, 9W), see Figure 2. For the comparison, both time series (Figure 2a) and scatterplots (Figure 2b) are presented. The AERONET observations represent measurement average within 15 minutes. To estimate the AOD at the AERONET site, the AOD retrieved with SARA over the ocean (spatial resolution of about 5 × 7 km^2 over Central Europe), has been averaged over an area of 10 km radius around the Cabo da Roca location. Although the SARA retrievals were analyzed on a three day period, the time series are presented only for 7 August 2006, to better show diurnal variations. The scatterplot comprises the results for the entire period from 6 to 8 August 2006. In the time series for 7 August, a maximum of 0.4 in the AOD (635 nm) was observed at Cabo da Roca around 13:00 (UTC), when the edge of the smoke plume crossed over the AERONET station. The AOD estimated from SARA shows a good agreement with AERONET, and the diurnal variations of the AOD are very well reproduced at all wavelengths. The correlation coefficient between SARA retrievals and AERONET is about 0.9 for the visible wavelengths. The correlation is weaker for the near-infrared channel, because small particles have less impact on the measurement at longer wavelengths. The AOD retrieved with SARA for the SEVIRI solar channels is overestimated, with a positive bias of about 0.06 to 0.08. The largest differences between SARA retrievals and AERONET are observed under low optical depth conditions (AOD < 0.1), as measured from AERONET. Under larger aerosol optical depth conditions (AOD > 0.1), the bias between AERONET and SEVIRI decreases. Although the comparison between MODIS and SEVIRI will be detailed in the next section, it can already be

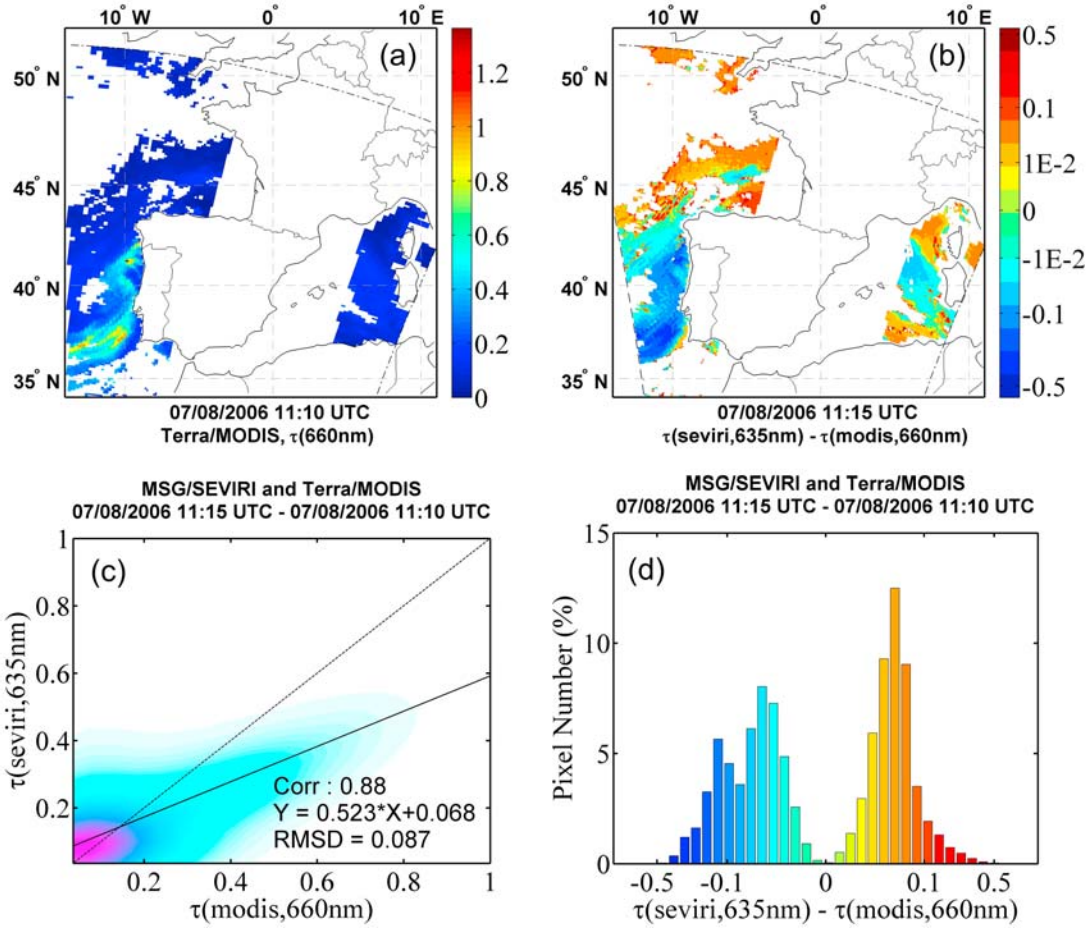

Figure 3. (a) Map (resolution ~10 × 10 km^2) of AOD at 660 nm ("best" solution) from MODIS aerosol product, and comparison of the retrieved AOD from MSG-SEVIRI (11:15 UTC) and MODIS (11:10 UTC), for the smoke plume from forest-fires in Portugal advected over the Atlantic Ocean on 7 August 2006. (b) Map of the AOD difference (resolution ~5 × 5 km^2). (c) Density scatterplot, with the correlation coefficient, the linear regression coefficients, and the root mean square difference. The dashed line represents the identity line, and the solid line is the calculated regression line. (d) Histogram of the AOD difference.

seen on this graph that the corresponding AOD retrieved from MODIS is largely overestimated in the visible bands.

4.1.3. Comparison With MODIS

[23] For this forest-fire case study, MODIS coincident overpass and SEVIRI observation were within 5 minutes. AOD spatial patterns for the first visible channel of SEVIRI are similar to those of the MODIS aerosol product at 660 nm (see Figure 3a). Over the ocean, the AOD at 660 nm derived from MODIS data, shows high optical depths along the west coast of the Iberian peninsula due to smoke advected from land over the Atlantic Ocean. The MODIS retrievals show that the smoke plume is mainly characterized by AOD values between 0.4 and 0.6, with higher values in the center of the plume exceeding 1. The AOD differences between the two instruments ($\tau_{seviri,635} - \tau_{modis,660}$) are presented in Figure 3. For this comparison, the AOD has not been adjusted to a common wavelength because an adjustment (using Ångström coefficient of 1) changes AOD by less than 10%. They are generally within ±0.1 with higher values in the tail of the distributions. The comparison analysis includes: the map (Figure 3b) and the histogram (Figure 3d) of the AOD differences, as well as the scatterplot (Figure 3c). The map of the AOD differences shows that in the plume the AOD estimated by SEVIRI is in general lower than the AOD estimated by MODIS, and visa versa outside the plume. This explains the double-peak feature of the histogram. These differences can reach values between −0.1 and −0.2 in the middle of the plume. However, about 80% of the pixels differ by less than 0.05. The largest positive differences (>0.4) are located on cloud edges and can therefore be ascribed to imperfections in the SARA cloud screening. The density scatterplot in Figure 3c shows that there is a good correlation between the two data sets (~90%). As noticed in the comparison with AERONET at Cabo da Roca (see previous section), the scatterplot confirms that MODIS overestimates the AOD in the forest-fire case. In coastal areas, underestimation of water leaving reflectance can produce AOD overestimations. Suppressing the chlorophyll correction in the SEVIRI retrievals has lead to larger AOD values over the smoke plume, and to a better agreement between MODIS and

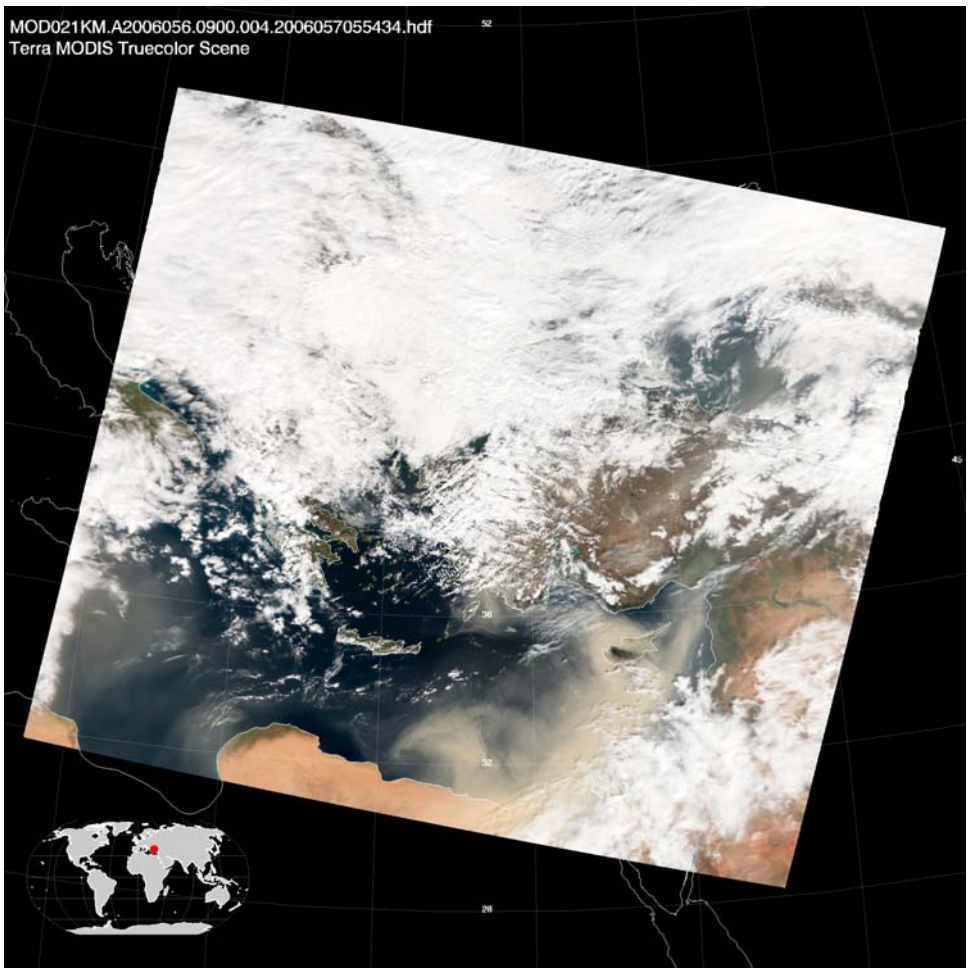

Figure 4. True color image from the MODIS Terra/Aqua collection for the dust storm over the Mediterranean Sea on 25 February 2006 as observed at 09:00 UTC.

SEVIRI. Therefore, MODIS overestimations may be caused by the differences in the surface reflectance correction.

4.2. Saharan Dust Storm Over the Eastern Mediterranean Sea

[24] The Mediterranean Sea is among the ocean areas with the highest aerosol optical depth in the world [*Prospero et al.*, 2002], especially during Saharan desert dust outbreaks. The Saharan desert is the major source of mineral aerosols on the Earth [*Papayannis et al.*, 2005], and dust aerosols have an important effect on climate [*Tanré et al.*, 2003], marine chemistry and sedimentation in the Mediterranean Sea [*Guerzoni and Chester*, 1996]. It is mostly transported in the form of seasonal "pulses" during the periods with high winds, and can be advected over long distances as a consequence of the injection to high altitudes up to 10 km [*Gobbi et al.*, 2000]. On February 25, 2006, a thick dust cloud was observed over the eastern Mediterranean Sea. It originated from a dust storm in the Saharan Desert that had started two days before. The MODIS RGB image (see Figure 4) shows a dense dust layer extending northwestward over the eastern Mediterranean. The dust obscures entirely the island of Cyprus, and heads from Libya and Egypt toward the Greek Islands. As is often observed during heavy dust events, atmospheric turbulence has produced several wave patterns which can be observed on the western edge of the plume.

4.2.1. Dust Detection

[25] In the presence of desert dust over the ocean, the cloud detection algorithm flags the dust-covered areas as cloudy. Therefore, an additional test has been added to discriminate water and ice clouds from dust clouds over the ocean. Dust constituents have absorption bands at wavelengths in the thermal infrared [*Sokolik et al.*, 2001], and as a result the brightness temperature difference between the 11 and 12 μm channels is generally negative, which is often not the case for liquid water clouds and ice clouds [*Duda et al.*, 2006]. For thin dust layers, the brightness temperature difference is small, and distinguishing between thin cirrus clouds and a thin layer of dust is difficult [*DeSouza-Machado et al.*, 2006].

[26] Dust pixels are not flagged as cloudy by the Infrared Gross Temperature Test (test 1), only by the Dynamic Visible Test (test 3) and/or the Dynamic Ratio Test (test 4) [cf. *Bennouna et al.*, 2009] for description of these tests). Both cloud tests 3 and 4 screen dense dust layers (middle of the plume), whereas for hazy dust regions (i.e. around a plume) only test 3 falsely indicates cloud contamination. Therefore two different flags for either "Dense Dust" or "Thin Dust" detection are used. When a pixel is classified

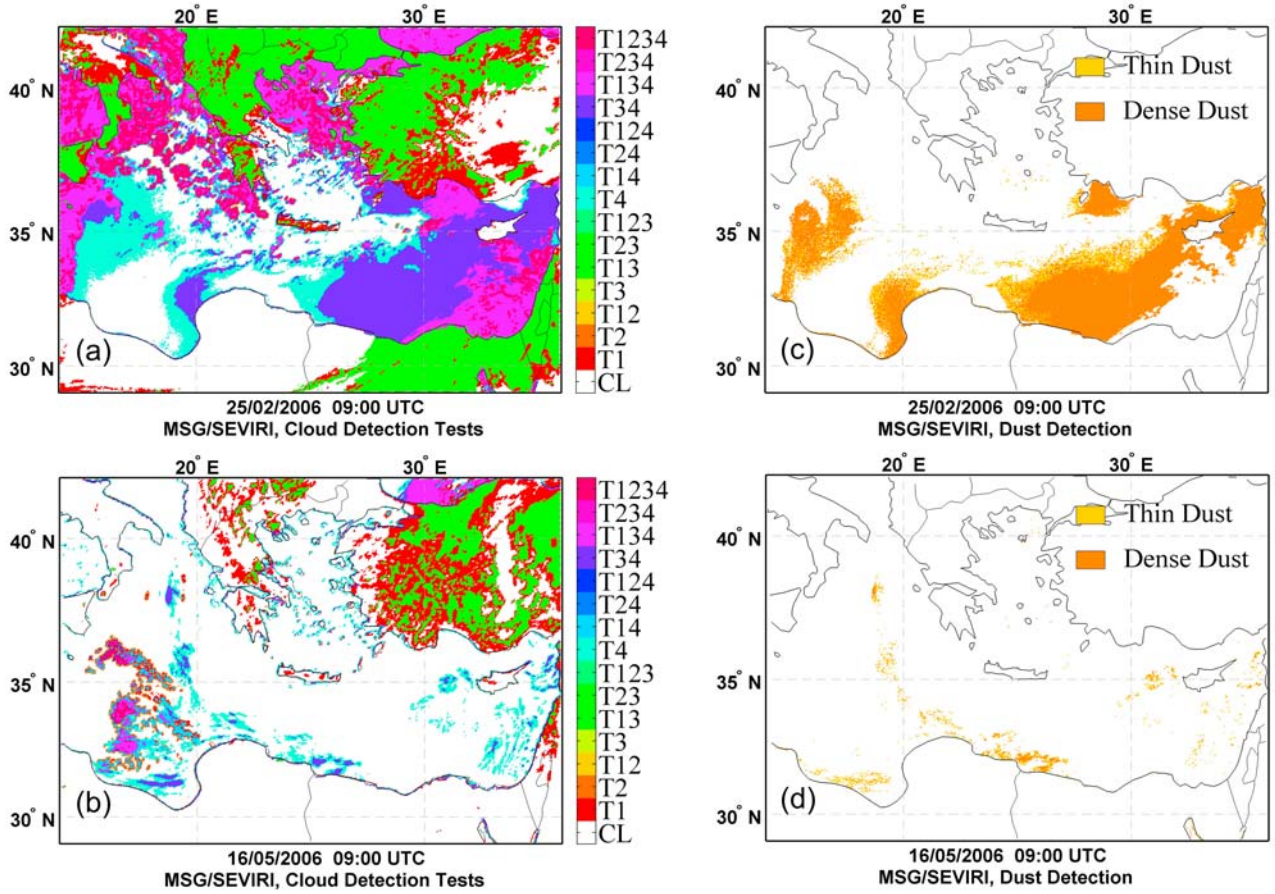

Figure 5. Cloud and dust detection results from SARA algorithm for the dust storm over the Mediterranean Sea on 25 February 2006 at 09:00 UTC. (a and b) Cloud mask and (c and d) dust detection maps. See text for further explanation. The cloud tests indicated on the color bar in Figures 5a and 5b are described by *Bennouna et al.* [2009].

as "clear" by test 1, and as "cloudy" by test 4 and/or test 3, the dust detection process is applied. In addition, it was observed that for similar features of reflectance and brightness temperature differences, dust tends to have a higher 12 μm brightness temperature than clouds. Thus, if the brightness temperature difference of this pixel is below 0.5 K, and if its 12 μm temperature is at least 2 K above the automatic temperature threshold determined by test 1, the "Dense Dust" flag is set positive. If the temperature difference is between 0.5 K and 0.7 K, and if the temperature of the pixel is at least 4 K higher than the threshold of test 1, the "Thin Dust" flag is set positive. In all other cases the dust detection result is negative. Figure 5 displays the cloud mask obtained, and the results from the dust detection process for both the dust storm case (Figures 5a and 5c), and for a clear day in the absence of dust (Figures 5b and 5d). As can be seen from Figure 5, the situation was very cloudy during the dust storm event, and the dust detection allowed to isolate the dust plume, as well as the thin layer of dust spread in the plume's surroundings (~7% of the pixels in total). The clear situation shows the presence of minor false detections of dust due to the presence of thin warm clouds. However, these detections, by their number (<1% of the pixels), and by the fact they are rather dispersed across the entire study area, already give an indication of wrong dust detection. In this case the dust flag must not be used to reset to clear pixels which have been screened in the cloud detection process.

4.2.2. SEVIRI Retrieval Results

[27] The AOD retrievals for SEVIRI were performed using different aerosol models. For one simulation the fine mode is based on the 'NAMb1' (water soluble), and the algorithm chooses the best coarse mode among 'NAMsoc' (sea salt), 'MODc8' and 'MODc9' (desert dust). For the other simulation, the different aerosol types of the 'OPAC' set are used (cf. section 2.3.1). In the latter, the fine mode is based on the 'OPACwaso' (water soluble), and the algorithm chooses the best coarse mode among 'OPACssam' (sea salt), 'OPACmiam' and 'OPACmitr' (desert dust). Since the simulations based on the OPAC aerosol models are not very satisfying, the results presented in Figure 6 were obtained with the simulation using NAM and MODIS aerosol models. For most aerosols the near-infrared AOD is rather low, except for large particles such as dust. Figure 6a shows the AOD map retrieved using SARA for the near-infrared channel of SEVIRI. The AOD at 1640 nm indicates large values in the plume off the Egyptian coast, which is therefore identified as a dust cloud. In the center of the dust cloud, the AOD reaches values as high as 5. For this case study, the Ångström coefficient is calculated between the

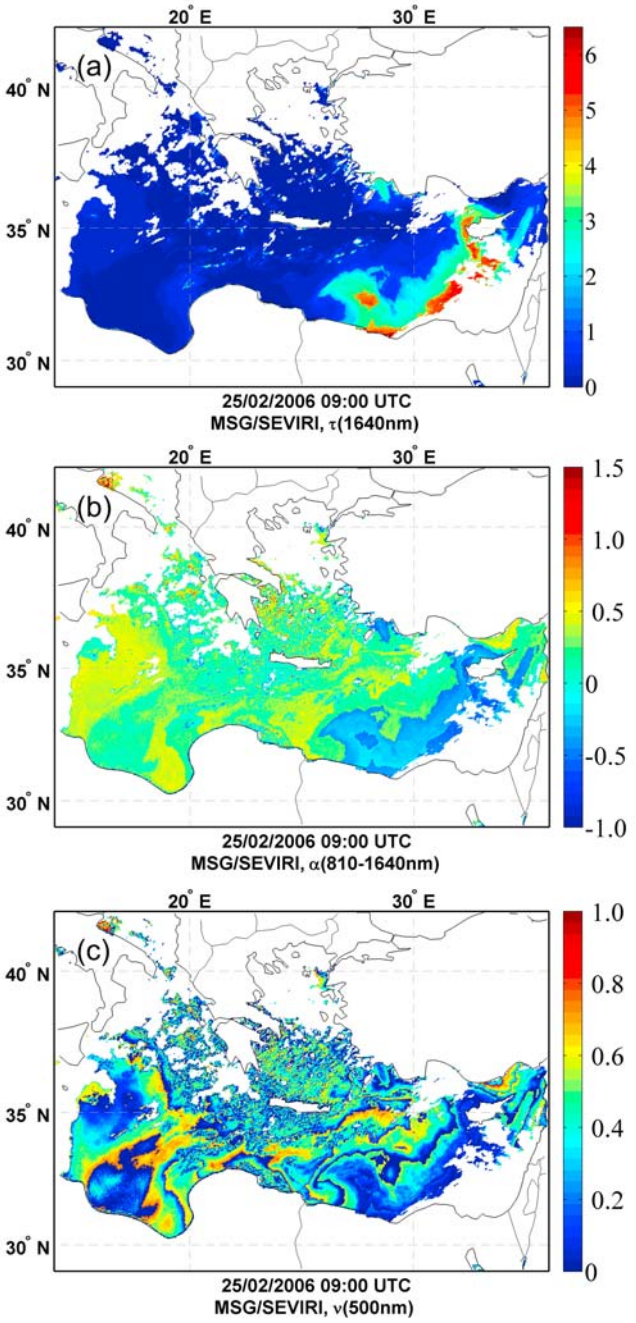

Figure 6. Results from SARA retrievals for the dust storm over the eastern Mediterranean on 25 February 2006 at 09:00 UTC. Maps (resolution $\sim 5 \times 7$ km^2) show (a) AOD at 1640 nm, (b) Ångström coefficient 810–1640 nm, and (c) weight of the fine/coarse mode aerosol on AOD at 500 nm.

wavelengths 810 nm and 1640 nm. The spatial distribution of the Ångström coefficient is shown in Figure 6b. Low values of the Ångström coefficients indicate the presence of large particles. In the areas where the dust is densest, the Ångström coefficient is negative, with values reaching a minimum of −0.5. Around the dust plume, the Ångström coefficient mostly ranges between 0 and 0.5. Values close to 0 can be explained by the dominance of marine aerosol or dust, whereas higher Ångström coefficients can probably be associated with polluted air masses. Clean areas with very low optical depth, as well as the dust plume region have a weak contribution of the fine mode aerosol to the total AOD at 500 nm, as opposed to air masses affected by pollution where the Ångström coefficient is usually higher than 0.5 (see Figure 6c).

4.2.3. Validation With AERONET

[28] Data from the AERONET station at Forth Crete (35N, 25E), located on the northeast coast of the Greek island of Crete, were used to validate the ocean retrieval results for the dust event. The comparison with AERONET is presented in Figure 7, with time series and scatterplots of results from a three day period from 24 to 27 February 2006. The SEVIRI AOD is presented as the average value for pixels at a distance of less than 10 km from the station. As for the results presented in the previous section, the comparison is shown only for SARA retrievals using the NAM/MODIS sets of aerosol models (fine: 'NAMb1',

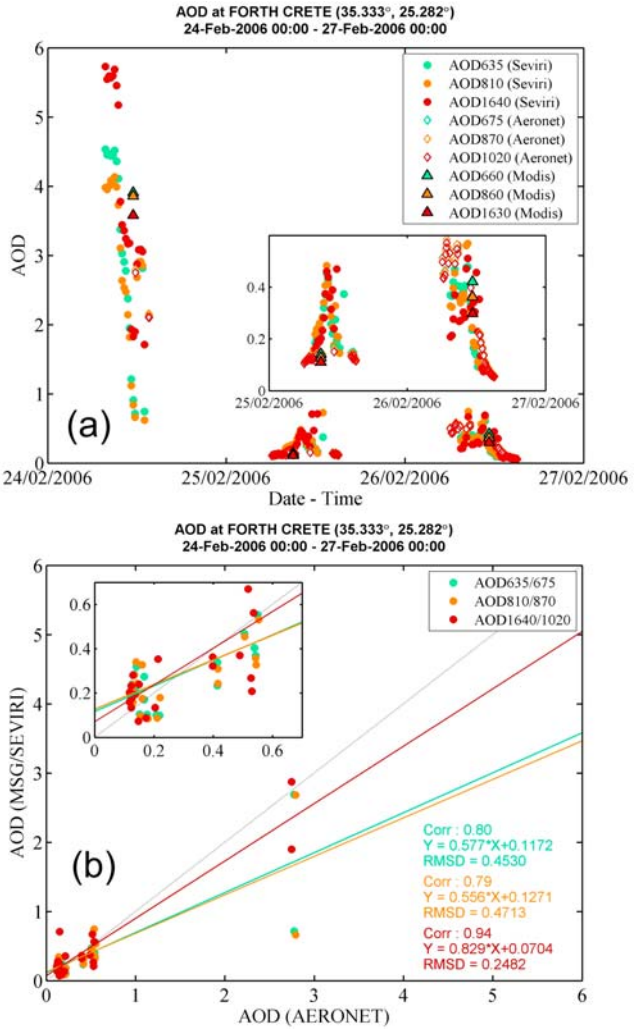

Figure 7. Comparison of the AOD retrieved using SARA with AERONET data at Forth Crete for the period 24–26 February 2006. (a) Time series (26 February 2006). (b) Scatterplots (24–26 February 2006). In Figure 7a the open diamonds stand for AERONET data, the dots represent SARA retrievals, and the triangles are the aerosol product for the MODIS overpass.

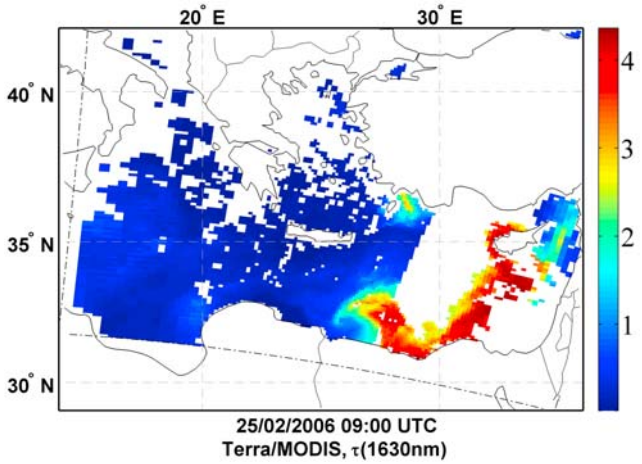

Figure 8. Map (resolution ~10 × 10 km^2) of AOD at 1630 nm ("best" solution) from MODIS aerosol product for the dust storm over the Mediterranean Sea on 25 February 2006 as observed at 09:00 UTC.

coarse: 'NAMsoc', 'MODISc8', 'MODISc9'). The time series in Figure 7a shows that the general trends in the AOD measured at Forth Crete and retrieved by SARA are similar. Some high frequency variations in the SARA AOD, which are not observed in the AERONET data, are probably due to cloud contamination. The scatterplot in Figure 7b shows that there is >79% correlation between AOD retrieved with SARA and AERONET measurements, and the best agreement between the two data sets is found for the near-infrared channels (94% correlation) with a slope of about 0.83 and a bias of 0.07. In Figure 7b, SARA retrievals appear unable to reproduce optical depth below 0.15 as measured by AERONET, which are highly overestimated. For the visible wavelengths, the AOD retrieved is much lower than the AOD from AERONET, whereas the near-infrared AODs are in good agreement. This could be caused by the aerosol modes used in the aerosol models.

4.2.4. Comparison With MODIS

[29] The results from SARA for the dust event were compared to the MODIS retrievals for the overpass at 09:00 (UTC) on the 25th of February. The map in Figure 8 shows the MODIS derived AOD at 1630 nm, which reaches values as high as 4 over the dust plume. In the area surrounding the dust, the AOD is between 1 and 2. These values are similar to those retrieved using SARA for a wavelength of 1640 nm, except for some areas in the center of the dust cloud where the AOD is lower in MODIS retrievals. Figure 9 shows the differences between the two products ($\tau_{seviri,1640} - \tau_{modis,1630}$). For the first comparison (Figures 9a, 9b, and 9c), SARA retrievals used aerosol types from NAM/MODIS sets, and for the second comparison (Figures 9d, 9e, and 9f) aerosol types from the OPAC set.

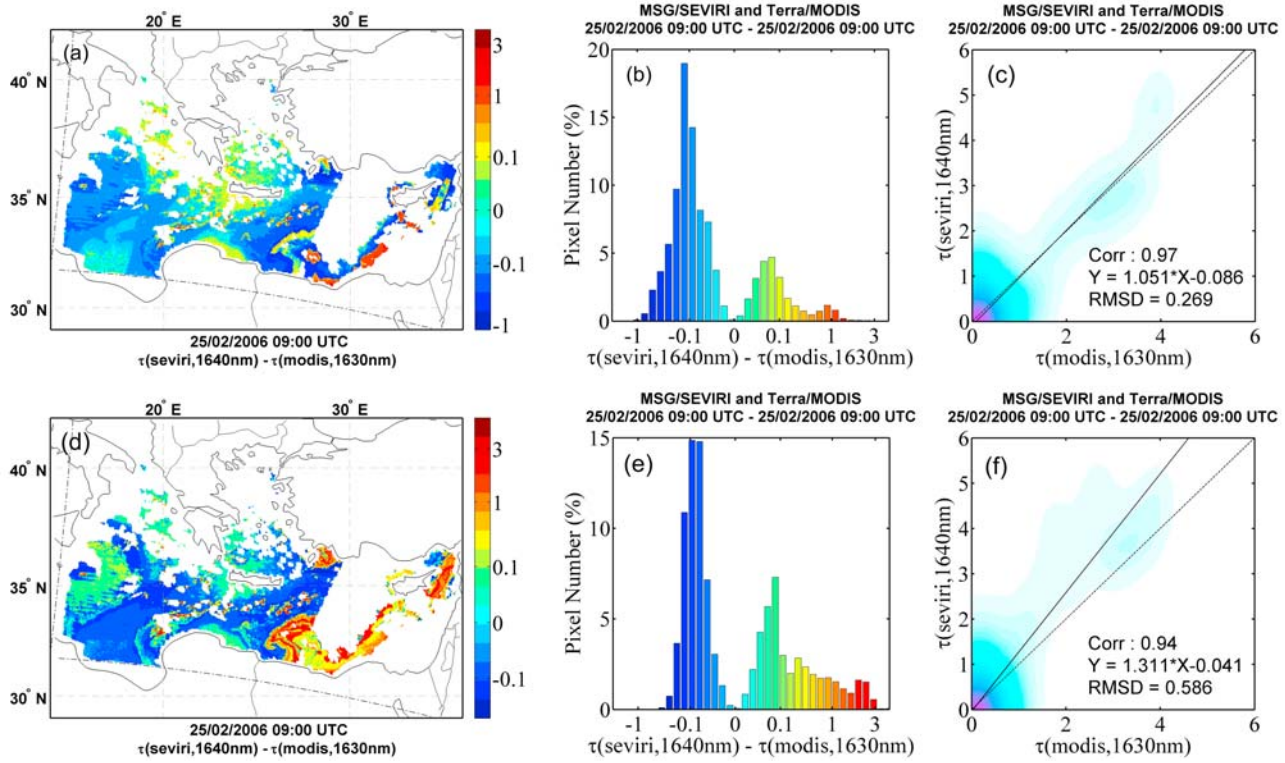

Figure 9. Comparison of the retrieved AOD from MSG-SEVIRI and MODIS, for the dust storm over the Mediterranean Sea on 25 February 2006 at 09:00 UTC. (a and d) Map of the AOD difference (resolution ~5 × 5 km^2). (b and e) Histogram of the AOD difference. (c and f) Density scatterplot, with indication for the correlation coefficient, the linear regression coefficients, and the Root Mean Square Difference. Figures 9a–9c are related to SARA retrievals obtained using both NAM and MODIS data sets, and Figures 9d–9f are related to SARA retrievals obtained using the OPAC data set. The dashed line in Figures 9c and 9f represents the identity line, and the solid line is the calculated regression line.

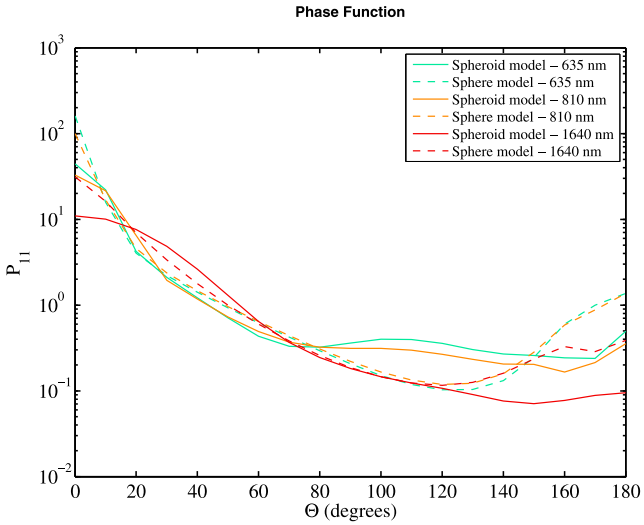

Figure 10. Phase function (P_{11}) of desert dust as a function of scattering angle (Θ), simulated for a sphere (dashed lines) and a spheroid model (solid lines) with a single axis ratio of 2. The different colors indicate the wavelengths of the SEVIRI channels for which the phase function is represented.

Like for the forest-fire case, the maps of the AOD difference (Figures 9a and 9d), the histograms of the AOD differences (Figures 9b and 9e), as well as the scatterplots (Figures 9c and 9f) are presented. The map of the AOD differences shows different patterns depending on the aerosol models that were used for the retrieval with SARA. In general, the first simulation (i.e. NAM/MODIS) seems to minimize the differences with the MODIS data, and for both simulations (i.e. NAM/MODIS and OPAC), the absolute difference is largest within the plume region. The differences observed over the dust plume are larger when the OPAC model is used. Outside the plume, large positive differences located on the edge of the cloud mask indicate the presence of cloud contaminated pixels in SARA retrievals. The rough shape of the histogram is similar for the two different simulations. About 70% of the pixels have an absolute difference smaller than 0.1 for the first SARA simulation. For the OPAC results, this percentage is slightly lower. The density scatterplots show that MODIS and SEVIRI retrievals are well correlated. The correlation coefficient is larger than 95% for the two simulations, and a consistently better agreement is found with the solution based on the MODIS dust aerosol model. The RMSD value is nearly doubled with the OPAC model. The coefficients of the linear regression confirm that AOD values retrieved with SARA are slightly higher than the results obtained with the MODIS algorithm. This difference is negligible in the first simulation, but it represents about 30% of the optical depth when the aerosol model is based on the OPAC. In the second simulation, it was noticed that the algorithm failed to distinguish sea salt from dust particles. This leads to discontinuities in the AOD retrieved over the dust plume. This may also explain the large overestimation of the AOD when the OPAC aerosol models are used. The linear regression between MODIS and SEVIRI retrievals indicates a very good agreement for SARA retrievals using NAM/MODIS aerosol models. The AOD value for the MODIS pixel coincident with the Forth Crete location is shown in the AERONET comparison described in the previous section (see Figure 7a). For the dust outbreak case, both MODIS and SARA retrievals present satisfactory agreement with AERONET.

4.2.5. Nonspherical Simulations

[30] The effect of particle shape on the retrieval of dust-like tropospheric aerosols is a crucial issue in aerosol remote sensing [*Koepke and Hess*, 1988]. The wrong assumption of particle sphericity can lead to large errors in retrievals of dust aerosol optical properties [*Mishchenko et al.*, 1995; *von Hoyningen-Huene and Posse*, 1997; *Mishchenko et al.*, 2003]. The phase function of desert dust aerosols can be modeled using a mixture of spheroids [*Mishchenko et al.*, 1997] characterized by a certain shape distribution. Inversions from AERONET Sun photometer measurements have shown that in desert dust plumes the number of particles in the coarse mode with a high aspect ratio dominates [*Dubovik et al.*, 2006].

[31] For the dust storm event presented in this paper, a very simple non-spherical model of randomly oriented spheroids was applied. The single scattering albedo and the expansion coefficients of the scattering matrix for the non-spherical model were calculated with the T-matrix code [*Mishchenko et al.*, 1996; *Mishchenko and Travis*, 1994]. No shape distribution was used, all particles are assumed to be prolate spheroids with the same shape. The shape aspect of the spheroids is parameterized by their axis ratio which is set to 2. The size distribution used for the spheroid model is based on the Gaussian size distribution used for the spherical model by preserving the volume of the spherical particles. For the dust aerosol model labeled 'MODISc8', the phase function calculated with the T-matrix code (i.e. spheroid model) is compared to the phase function obtained with the MIE code (i.e. spherical model) in Figure 10. For the three SEVIRI wavelengths, the spheroid and the spherical model differ mainly in their phase function at large scattering angles (160°–180°). As compared to the sphere model, the curve flattens at large scattering angles in the nonspherical case, therefore the back scattered intensity is smaller for these geometries.

[32] Similarly to simulations made with the sphere model, two non-spherical dust aerosol models labeled as 'MODISc8' and 'MODISc9' were used to retrieve the AOD with SARA. The results obtained with the nonspherical retrievals are presented in Figure 11. In general, the spatial variations obtained with the non-spherical model are similar to those obtained with the spherical simulations. However, the AOD observed over the dust plume is lower by approximately 25% than for the spherical simulations (see Figure 11a). This can be explained by considering the scattering angles encountered in the retrieval, which are in the range of 129° to 133°. For these angles, the scattered intensities of nonspherical particles at 635 nm and 810 nm are significantly larger than those of the spherical one, and thus the AOD retrieved in these channels is smaller for nonspherical particles (not shown). In contrast, for the 1640 nm channel, the scattered intensities of the spheroid model is slightly smaller than the spherical one. As a consequence, the AOD at 1640 nm should be slightly larger

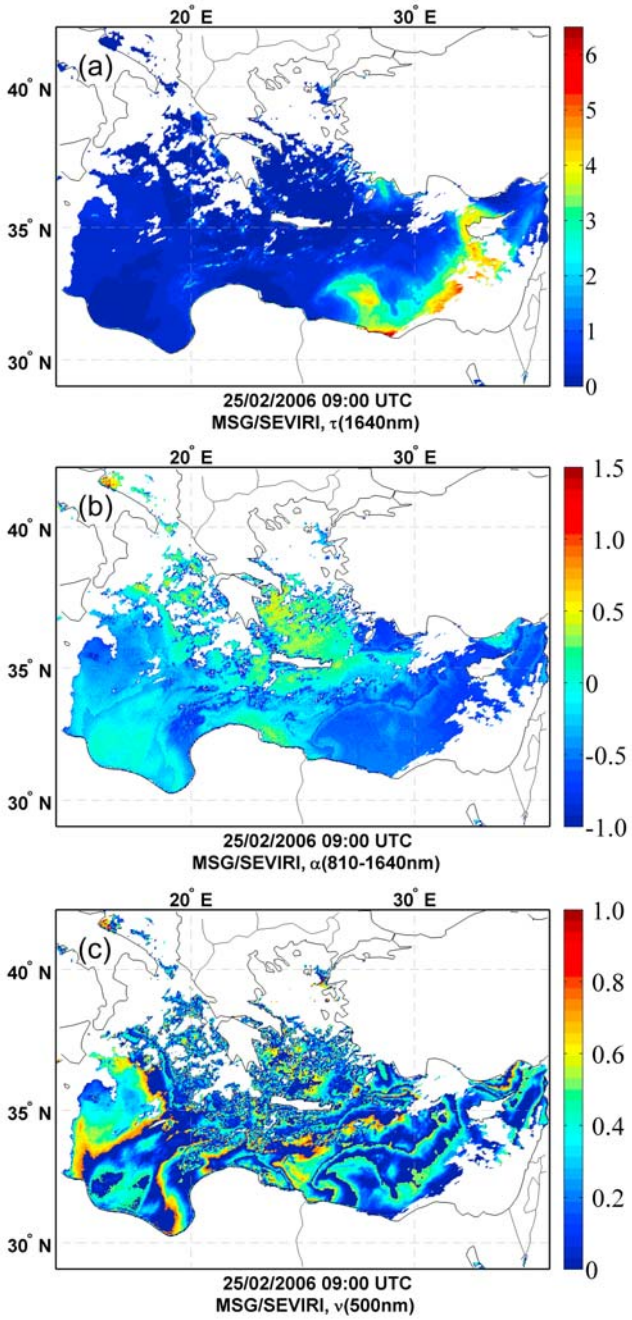

Figure 11. Results from SARA retrievals for the dust storm over the eastern Mediterranean on 25 February 2006 at 09:00 UTC. Maps (resolution $\sim 5 \times 7$ km^2) show (a) AOD at 1640 nm, (b) Ångström coefficient 810–1640 nm, and (c) weight of the fine/coarse mode aerosol on AOD at 500 nm.

for the spheroid model than for the spherical one, whereas, as mentioned before, the contrary is observed. This intensity difference between the spheroid and the spherical model at 1640 nm seems somewhat compensated by the higher single scattering albedo of the spheroid model than that of the spherical one at this wavelength. The map of the Ångström coefficients (see Figure 11b) shows a less clear distinction between the oceanic background and the dust cloud than in the spherical case. Although the values of Ångström coefficient are nearly homogeneous over the area, they are slightly lower over the dusty regions (<-0.2) than over clean areas (>0). As regards the weight of the fine/coarse mode on the AOD at 500 nm (see Figure 11c), the maps for the spherical and the non-spherical simulations are very similar, the differences do not exceed 5%. For the comparison with MODIS, in Figure 12, the map and the histogram of the AOD differences are similar to the results obtained for the spherical simulations. In the considered range of scattering angles, the phase function of the spherical and the spheroid model are indeed much alike at 1630 nm. It should be noted that the differences between spherical and non-spherical retrievals from SARA are more notable at 635 nm and 810 nm (not shown). Although the differences in the phase function between the spherical and the spheroid models are of little importance in the near-infrared, the comparison of the scatterplots in Figures 9c and 12c shows that a better agreement is found between MODIS and SARA results when the nonspherical model is used, in particular for the highest AOD values.

5. Conclusions

[33] The approach used in the AATSR aerosol retrieval algorithm over the ocean has been applied to the data from the MSG-SEVIRI instrument through the implementation of the new algorithm SARA. Several sets of LUTs for use with SARA and based on different aerosol models were produced with the DAK radiative transfer model. The results obtained with SARA based on these pre-computed LUTs have demonstrated its capability to derive optical properties such as the aerosol optical depth and the Ångström coefficient over the ocean for case studies related to forest fires and dust storm.

[34] During the summer of 2006, a forest fire episode in Spain and Portugal has resulted in high AOD values over the Atlantic coast of the Iberian peninsula. The values of AOD retrieved with SARA have been validated against AERONET 'ground-truth' measurements for the coastal station of Cabo da Roca, and showed ~90% correlation in the visible channels. The diurnal variation of the retrievals at the AERONET location are in very good agreement with the AERONET trends (bias of about 0.07). Comparison with MODIS shows that the spatial variations of the AOD over the ocean are well reproduced by the SARA algorithm with approximately 87% correlation. Other parameters derived from the retrievals, such as the Ångström coefficient and the contribution of the fine mode to the total AOD at 500 nm, provide information which confirms the dominance of fine aerosol particles in the smoke plume and their important contribution to the total AOD at 500 nm.

[35] The second case study is related to the dust outbreak over the eastern Mediterranean in February 2006. This case study required the implementation of a desert dust detection routine which provides a satisfactory discrimination between dust and clouds over the ocean for the studied event. The AOD retrieved using SARA is in very good agreement with MODIS retrievals, which is further improved by using a nonspherical model to represent the coarse mode for the dust aerosol type: 98% correlation and a bias of about 0.02

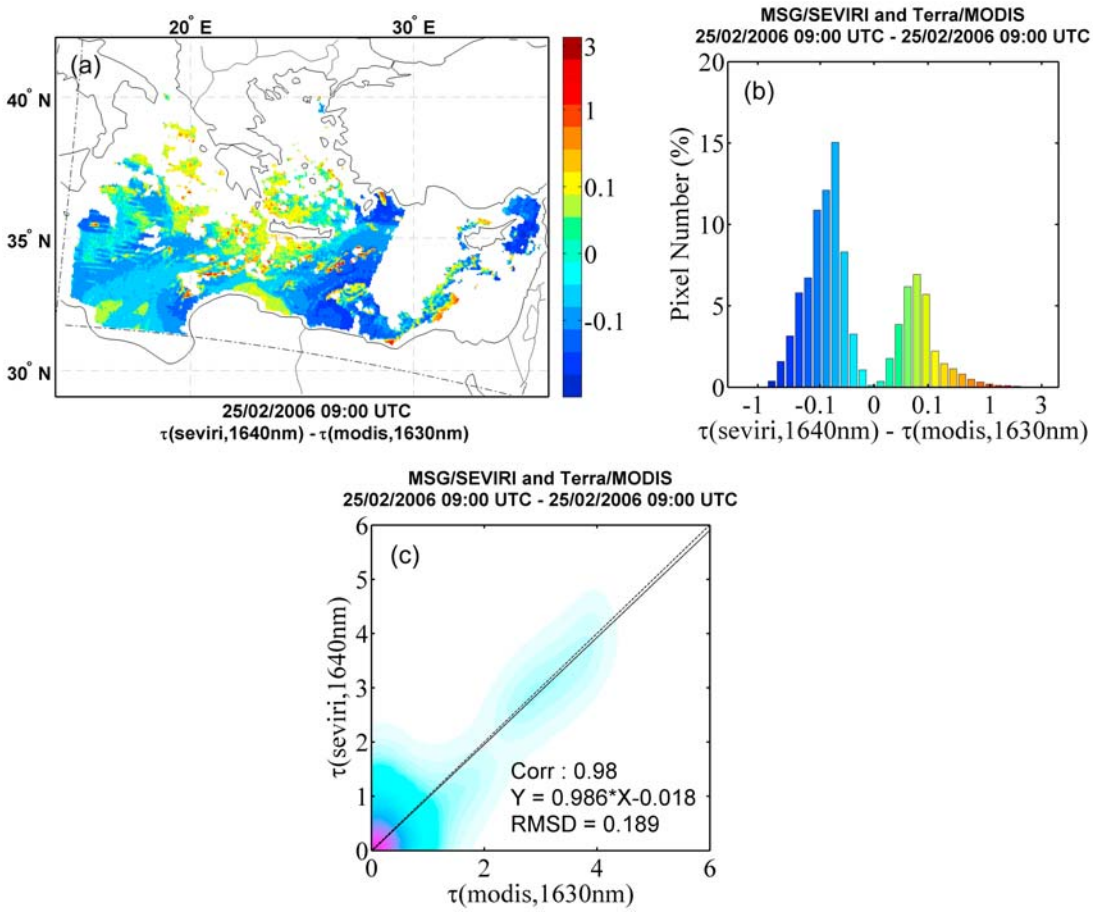

Figure 12. Comparison of the retrieved AOD from MSG-SEVIRI and MODIS, for the dust storm over the Mediterranean Sea on 25 February 2006 at 09:00 UTC, with the use of a nonspherical dust model. (a) Map of the AOD difference (resolution $\sim 5 \times 5$ km^2). (b) Histogram of the AOD difference. (c) Density scatterplot, with indication for the correlation coefficient, the linear regression coefficients, and the root mean square difference. The dashed line represents the identity line, and the solid line is the calculated regression line.

for the near-infrared channel. For the desert dust case study, no solid conclusions could be drawn from the comparison with the ground measurement time series, due to the presence of clouds. However, the general trends of the AOD provided by SARA retrievals agree reasonably with observations made at the AERONET site of Forth Crete. According to the Ångström coefficient derived from the retrievals, the coarse mode was found dominant where the dust was densest, and its fraction vanished as the dust was mixing with the surrounding polluted air masses. Due to the particular range of scattering angles, non-spherical and spherical simulations produced similar results for the near-infrared wavelength in this study. The impact of using this non-spherical model in SARA retrievals over the ocean should be further investigated with applications to other desert dust events presenting different illumination-observation geometries. Moreover, when non-spherical aerosol types were used for dust, the algorithm preferentially chose one size among the two coarse modes (i.e. 'MODISc8' or 'MODISc9'). So both the size and phase function of the aerosol a priori play an important role in the determination of the 'best' aerosol model in the algorithm. The values of the retrieved AOD are found not significantly dependant on the aerosol model. Meanwhile the ability to retrieve the aerosol type certainly requires further development and additional studies.

[36] **Acknowledgments.** The authors would like to thank the KNMI for providing the SEVIRI data. We express our gratitude to the Aerosol Robotic Network (AERONET) and the principal investigators of the different sites, as well as the NASA and the MODIS Science Teams for making available the aerosol data used in this study. Financial support from the SRON (project EO-077) is gratefully acknowledged.

References

Baker, K. S., and R. C. Smith (1982), Bio-optical classification and model of natural waters. 2, *Limnol. Oceanogr.*, *27*(3), 500–509.

Bennouna, Y. S., R. L. Curier, G. de Leeuw, J. Piazzola, R. Roebeling, and P. de Valk (2009), An automated day-time cloud detection technique applied to MSG-SEVIRI data over Western Europe, *Int. J. Remote Sens.*, in press.

Brindley, H. E., and A. Ignatov (2006), Retrieval of mineral aerosol optical depth and size information from Meteosat Second Generation SEVIRI solar reflectance bands, *Remote Sens. Environ.*, *102*(3–4), 344–363.

Campbell, J. W., J. M. Blaisdell, and M. Darzi (1995), Level-3 SeaWiFS Data Products: Spatial and Temporal Binning Algorithms, *NASA Tech. Memo, 104566*, 73 pp.

Chu, D. A., Y. J. Kaufman, C. Ichoku, L. A. Remer, D. Tanré, and B. N. Holben (2002), Validation of MODIS aerosol optical depth retrieval over land, *Geophys. Res. Lett.*, *29*(12), 8007, doi:10.1029/2001GL013205.

Cox, C., and W. Munk (1954), Measurement of the roughness of the sea surface from photographs of the Sun's glitter, *J. Opt. Soc. Am.*, *44*, 838–850.

Curier, R. L., G. de Leeuw, P. Kolmonen, A.-M. Sundstrm, L. Sochageva, and Y. Bennouna (2009), Aerosol retrieval over land using the ATSR dual-view algorithm, in *Satellite Aerosol Remote Sensing Over Land*, edited by A. A. Kokhanovsky and G. de Leeuw, pp. 135–159, Springer-Praxis, Berlin.

DeCarlo, P., J. G. Slowik, D. R. Worsnop, P. Davidovits, and J. L. Jimenez (2004), Particle morphology and density characterization by combined mobility and aerodynamic diameter measurements. Part 1: Theory, *Aerosol Sci. Technol.*, *38*(12), 1185–1205.

de Haan, J. F., P. B. Bosma, and J. W. Hovenier (1987), The adding method for multiple scattering calculations of polarized light, *Astron. Astrophys*, *183*, 371–391.

de Leeuw, G., K. L. Davidson, S. G. Gathman, and R. V. Noonkester (1989), Modeling of aerosols in the marine mixed-layer, *Proc. SPIE Int. Soc. Opt. Am.*, *1115*, 287–294.

De Paepe, R., A. Ignatov, S. Dewitte, and A. Ipe (2008), Aerosol retrieval over ocean from SEVIRI for the use in GERB Earth's radiation budget analyses, *Remote Sens. Environ.*, *112*(5), 2455–2468.

de Rooij, W. A., and C. van der Stap (1984), Expansion of Mie scattering matrices in generalized spherical functions, *Astron. Astrophys*, *131*, 237–248.

DeSouza-Machado, S. G., L. L. Strow, S. E. Hannon, and H. E. Motteler (2006), Infrared dust spectral signatures from AIRS, *Geophys. Res. Lett.*, *33*, L03801, doi:10.1029/2005GL024364.

Deuzé, J. L., M. Herman, P. Goloub, D. Tanré, and A. Marchand (1999), Characterization of aerosols over ocean from POLDER/ADEOS-1, *Geophys. Res. Lett.*, *26*(10), 1421–1424.

Deuzé, J. L., et al. (2001), Remote sensing of aerosols over land surfaces from POLDER-ADEOS-1 polarized measurements, *J. Geophys. Res.*, *106*(D5), 4913–4926.

Dubovik, O., and M. D. King (2000), A flexible inversion algorithm for retrieval of aerosol optical properties from sun and sky radiance measurements, *J. Geophys. Res.*, *105*(D16), 20,673–20,696.

Dubovik, O., et al. (2006), Application of spheroid models to account for aerosol particle nonsphericity in remote sensing of desert dust, *J. Geophys. Res.*, *111*, D11208, doi:10.1029/2005JD006619.

Duda, D. P., P. Minnis, Q. Trepte, and S. Sun-Mack (2006), The continuous monitoring of desert dust using an infrared-based dust detection and retrieval method, paper presented at 12th Conference on Atmospheric Radiation, Am. Meteorol. Soc., Madison, Wis.

Durkee, P. A., D. R. Jensen, E. E. Hindman, and T. H. Vonder Haar (1986), The relationship between marine aerosol particles and satellite-detected radiance, *J. Geophys. Res.*, *91*, 4063–4072.

Flossmann, A. I. (1998), Interaction of aerosol particles and clouds, *J. Atmos. Sci.*, *55*(5), 879–887.

Fresnel, A. (1827), Elementary view of an ondulatory theory of light, *Q. J. Sci.*, *23*, 127–141.

Gobbi, G. P., F. Barnaba, R. Giorgi, and A. Santacasa (2000), Altitude-resolved properties of a Saharan dust event over the Mediterranean, *Atmos. Environ.*, *34*(29–30), 5119–5127.

Gordon, H. R., and A. Morel (1983), *Remote Assessment of Ocean Color for Interpretation of Satellite Visible Imagery: A Review*, 114 pp., Springer, New York.

Gordon, H., J. Brown, O. Brown, R. Evans, and R. Smith (1988), A semianalytic radiance model of ocean color, *J. Geophys. Res.*, *93*(D9), 10,909–10,924.

Griggs, M. (1981), AVHRR measurements of atmospheric aerosols over oceans, final report, Sci. Appl., Inc., San Diego, Calif.

Guerzoni, S., and R. Chester (1996), *The Impact of Desert Dust Across the Mediterranean*, Kluwer Acad., Norwell, Mass.

Hess, M., P. Koepke, and I. Schult (1998), Optical Properties of Aerosols and Clouds: The software package OPAC, *Bull. Am. Meteorol. Soc.*, *79*(5), 831–844.

Holben, B. N., Y. J. Kaufman, T. F. Eck, I. Slutsker, D. Tanré, J. P. Buis, A. Setzer, E. Vermote, and J. Reagan (1998), AERONET—A federated instrument network and data archive for aerosol characterization, *Remote Sens. Environ.*, *66*(1), 1–16.

Ichoku, C., D. A. Chu, S. Mattoo, Y. J. Kaufman, L. A. Remer, D. Tanré, I. Slutsker, and B. N. Holben (2002), A spatio-temporal approach for global validation and analysis of MODIS aerosol products, *Geophys. Res. Lett.*, *29*(12), 8006, doi:10.1029/2001GL013206.

Intergovernmental Panel on Climate Change (IPCC) (2008), *Climate Change 2007: The Physical Science Basis. Contribution of Working Group I to the Fourth Assessment Report of the Intergovernmental Panel on Climate Change*, Cambridge, Univ. Press, Cambridge, U. K.

Kalashnikova, O. V., and I. N. Sokolik (2002), Importance of shapes and compositions of wind-blown dust particles for remote sensing at solar wavelengths, *Geophys. Res. Lett.*, *29*(10), 1398, doi:10.1029/2002GL014947.

Kaufman, Y. J., Y. J. D. Tanré, L. A. Remer, E. F. Vermote, A. Chu, and B. N. Holben (1997), Operational remote sensing of tropospheric aerosol over land from EOS moderate resolution imaging spectroradiometer, *J. Geophys. Res.*, *102*(D14), 17,051–17,067.

Kaufman, Y. J., D. Tanré, and O. Boucher (2002), A satellite view of aerosols in the climate system, *Nature*, *419*(6903), 215–223.

Kerker, M. (1969), *The Scattering of Light and Other Electromagnetic Radiation*, Academic Press, San Diego, Calif.

Koelemeijer, R., P. Stammes, J. Hovenier, and J. de Haan (2001), A fast method for the retrieval of cloud parameters using oxygen A-band measurements from the Global Ozone Monitoring Instrument, *J. Geophys. Res.*, *106*, 3475–3490.

Koepke, P. (1984), Effective reflectance of oceanic whitecaps, *Appl. Opt.*, *23*(11), 1816–1824.

Koepke, P., and M. Hess (1988), Scattering functions of tropospheric aerosols—The effects of nonspherical particles, *Appl. Opt.*, *27*(12), 2422–2430.

Kokhanovsky, A. A. (2004), Spectral reflectance of whitecaps, *J. Geophys. Res.*, *109*, C05021, doi:10.1029/2003JC002177.

Kokhanovsky, A. A., R. L. Curier, G. de Leeuw, W. M. F. Grey, K.-H. Lee, Y. S. Bennouna, R. Schoemaker, and P. R. J. North (2009), The inter-comparison of AATSR dual view aerosol optical thickness retrievals with results from various algorithms and instruments, *Int. J. Remote Sens.*, in press.

Kriebel, K. T., G. Gesell, M. Kästner, and H. Mannstein (2003), The cloud analysis tool APOLLO: improvements and validations, *Int. J. Remote Sens.*, *24*(12), 2389–2408.

Kuśmierczyk-Michulec, J., and G. de Leeuw (2005), Aerosol optical thickness retrieval over land and water using Global Ozone Monitoring Experiment (GOME) data, *J. Geophys. Res.*, *110*, D10S05, doi:10.1029/2004JD004780.

Levy, R. C., L. A. Remer, D. Tanré, Y. J. Kaufman, C. Ichoku, B. N. Holben, J. M. Livingston, P. B. Russell, and H. Maring (2003), Evaluation of the Moderate-Resolution Imaging Spectroradiometer (MODIS) retrievals of dust aerosol over the ocean during PRIDE, *J. Geophys. Res.*, *108*(D19), 8594, doi:10.1029/2002JD002460.

Levy, R. C., L. A. Remer, J. V. Martins, Y. J. Kaufman, A. Plana-Fattori, J. Redemann, and B. Wenny (2005), Evaluation of the MODIS Aerosol Retrievals over Ocean and Land during CLAMS, *J. Atmos. Sci.*, *62*(4), 974–992.

Levy, R. C., L. A. Remer, S. Mattoo, E. F. Vermote, and Y. Kaufman (2007), Second-generation algorithm for retrieving aerosol properties over land from MODIS spectral reflectance, *J. Geophys. Res.*, *112*, D13211, doi:10.1029/2006JD007811.

Martonchik, J. V., D. J. Diner, R. A. Kahn, T. P. Ackerman, M. M. Verstraete, B. Pinty, and H. R. Gordon (1998), Techniques for the retrieval of aerosol properties over land andocean using multiangle imaging, *IEEE Trans. Geosci. Remote Sens.*, *36*(4), 1212–1227.

Martonchik, J. V., D. J. Diner, K. Crean, and M. A. Bull (2002), Regional aerosol retrieval results from MISR, *IEEE Trans. Geosci. Remote Sens.*, *40*(7), 1520–1531.

McClatchey, R. A., R. W. Fenn, J. E. A. Selby, F. E. Volz, and J. S. Garing (1972), Optical properties of the atmosphere, *AFCRL-72-0497*, 108 pp., Air Force Cambridge Res. Lab., Bedford, Mass.

Mie, G. (1908), A contribution to the optics of turbid media, especially colloidal metallic suspensions, *Ann. Phys.*, *25*(4), 377–445.

Mishchenko, M. I., and L. D. Travis (1994), T-matrix computations of light scattering by large spheroidal particles, *Opt. Commun.*, *109*(1–2), 16–21.

Mishchenko, M. I., A. A. Lacis, B. E. Carlson, and L. D. Travis (1995), Nonsphericity of dust-like tropospheric aerosols: Implications for aerosol remote sensing and climate modeling, *Geophys. Res. Lett.*, *22*(9), 1077–1080.

Mishchenko, M. I., L. D. Travis, and D. W. Mackowski (1996), T-matrix computations of light scattering by nonspherical particles: A review, *J. Quant. Spectrosc. Radiat. Transfer*, *55*(5), 535–575.

Mishchenko, M. I., L. D. Travis, R. A. Kahn, and R. A. West (1997), Modeling phase functions for dustlike tropospheric aerosols using a shape mixture of randomly oriented polydisperse spheroids, *J. Geophys. Res.*, *102*(D14), 16,831–16,847.

Mishchenko, M. I., I. V. Geogdzhayev, L. Liu, J. A. Ogren, A. A. Lacis, W. B. Rossow, J. W. Hovenier, H. Volten, and O. Muñoz (2003), Aerosol retrievals from AVHRR radiances: effects of particle nonsphericity and absorption and an updated long-term global climatology of aerosol properties, *J. Quant. Spectrosc. Radiat. Transfer*, *79*, 953–972.

Monahan, E. C., and I. Ó. Muircheartaigh (1980), Optimal power-law description of oceanic whitecap coverage dependence on wind speed, *J. Phys. Oceanogr.*, *10*(12), 2094–2099.

Moore, K. D., K. J. Voss, and H. R. Gordon (2000), Spectral reflectance of whitecaps: Their contribution to water-leaving radiance, *J. Geophys. Res*, *105*(C3), 6493–6499.

Morel, A. (1988), Optical modeling of the upper ocean in relation to its biogenous matter content (case I waters), *J. Geophys. Res.*, *93*(C9), 10,749–10,768.

Morel, A., and B. Gentili (1996), Diffuse reflectance of oceanic waters. III. Implication of bidirectionality for the remote-sensing problem, *Appl. Opt.*, *35*(24), 4850–4862.

Morel, A., and L. Prieur (1977), Analysis of variations in ocean color, *Limnol. Oceanogr.*, *22*(4), 709–722.

Papayannis, A., D. Balis, V. Amiridis, G. Chourdakis, G. Tsaknakis, C. Zerefos, A. D. A. Castanho, S. Nickovic, S. Kazadzis, and J. Grabowski (2005), Measurements of saharan dust aerosols over the eastern mediterranean using elastic backscatter-raman lidar, spectrophotometric and satellite observations in the frame of the earlinet project, *Atmos. Chem. Phys. Discuss.*, *5*(2), 2075–2110. (Available at http://www.atmos-chem-phys-discuss.net/5/2075/2005/)

Prospero, J. M., P. Ginoux, O. Torres, S. E. Nicholson, and T. E. Gill (2002), Environmental characterization of global sources of atmospheric soil dust identified with the NIMBUS 7 Total Ozone Mapping Spectrometer (TOMS) absorbing aerosol product, *Rev. Geophys.*, *40*(1), 1002, doi:10.1029/2000RG000095.

Remer, L. A., et al. (2002), Validation of MODIS aerosol retrieval over ocean, *Geophys. Res. Lett.*, *29*(12), 8008, doi:10.1029/2001GL013204.

Remer, L. A., et al. (2005), The MODIS aerosol algorithm, products, and validation, *J. Atmos. Sci.*, *62*(4), 947–973.

Remer, L. A., D. Tanré, and Y. Kaufman (2006), Algorithm for remote sensing of tropospheric aerosol from MODIS: Collection 5, *OMI-ATBD-02*, NASA Goddard Space Flight Cent., Greenbelt, Md. (Available at http://modis.gsfc.nasa.gov/data/atbd/atbd\mod02.pdf)

Robles-Gonzalez, C. (2003), Retrieval of aerosol properties using ATSR-2 observations and their interpretation, Ph.D. thesis, Utrecht Univ., Utrecht, Netherlands.

Ruddick, K. G., V. De Cauwer, Y. J. Park, and G. Moore (2006), Seaborne measurements of near infrared water-leaving reflectance: The similarity spectrum for turbid waters, *Limnol. Oceanogr.*, *51*(2), 1167–1179.

Salomonson, V. V., W. L. Barnes, P. W. Maymon, H. E. Montgomery, and H. Ostrow (1989), MODIS: Advanced facility instrument for studies of the Earth as asystem, *IEEE Trans. Geosci. Remote Sens.*, *27*(2), 145–153.

Saunders, R. W., and K. T. Kriebel (1988), An improved method for detecting clear sky and cloudy radiances from AVHRR data, *Int. J. Remote Sens.*, *9*(1), 123–150.

Schmetz, J., P. Pili, S. Tjemkes, D. Just, J. Kerkmann, S. Rota, and A. Ratier (2002), An introduction to Meteosat Second Generation (MSG), *Bull. Am. Meteorol. Soc.*, *83*, 977–992.

Seinfeld, J. H., and S. N. Pandis (1998), Properties of atmospheric aerosols, in *Atmospheric Chemistry and Physics: From Air Pollution to Climate Change*, pp. 408–763, John Wiley, Hoboken, N. J.

Shettle, E. P., and R. W. Fenn (1979), Models for the Aerosols of the Lower Atmosphere and the Effects of Humidity Variations on their Optical Properties, *Environ. Res. Pap. A159580*, Air Force Geophys. Lab., Hanscom AFB, Mass.

Smith, R. C., and K. S. Baker (1978), The bio-optical state of ocean waters and remote sensing, *Limnol. Oceanogr*, *23*(2), 247–259.

Smith, R. C., and K. S. Baker (1981), Optical properties of the clearest natural waters (200–800 nm), *Appl. Opt.*, *20*(2), 177–184.

Sokolik, I. N., D. M. Winker, G. Bergametti, and D. Gillette (2001), Introduction to special section: Outstanding problems in quantifying the radiative impacts of mineral dust, *J. Geophys. Res.*, *106*(D16), 18,015–18,028.

Stammes, P. (2001), *Manual for the DAK program*, R. Neth. Meteorol. Inst., De Bilt, Netherlands.

Takashima, T., and K. Masuda (1985), Degree of radiance and polarization of the upwelling radiation from an atmosphere-ocean system, *Appl. Opt.*, *24*(15), 2423–2429.

Tanré, D., M. Herman, P. Y. Deschamps, and A. De Leffe (1979), Atmospheric modeling for space measurements of ground reflectances, including bidirectional properties, *Appl. Opt.*, *18*(21), 3587–3594.

Tanré, D., Y. J. Kaufman, M. Herman, and S. Mattoo (1997), Remote sensing of aerosol properties over oceans using the MODIS/EOS spectral radiances, *J. Geophys. Res.*, *102*(D14), 16,971–16,988.

Tanré, D., J. Haywood, J. Pelon, J. F. Leon, B. P. Chatenet, P. Francis Formenti, P. Goloub, E. J. Highwood, and G. Myhre (2003), Measurement and modeling of the Saharan dust radiative impact: Overview of the Saharan Dust Experiment (SHADE), *J. Geophys. Res.*, *108*(D18), 8574, doi:10.1029/2002JD003273.

Torres, O., P. K. Bhartia, J. R. Herman, A. Sinyuk, P. Ginoux, and B. Holben (2002), A long-term record of aerosol optical depth from TOMS observations and comparison to AERONET measurements, *J. Atmos. Sci.*, *59*(3), 398–413.

Twomey, S. (1977), The influence of pollution on the shortwave albedo of clouds, *J. Atmos. Sci.*, *34*(7), 1149–1152.

Twomey, S. A., M. Piepgrass, and T. L. Wolfe (1984), An assessment of the impact of pollution of global cloud albedo, *Tellus, Ser. B*, *36*, 356–366.

van de Hulst, H. C. (1957), *Light Scattering by Small Particles*, John Wiley, Hoboken, N. J.

Veefkind, J. P. (1999), Aerosol satellite remote sensing, Ph.D. thesis, Univ. of Utrecht, Utrecht, Netherlands.

Veefkind, J. P., and G. de Leeuw (1998), A new algorithm to determine the spectral aerosol optical depth from satellite radiometer measurements, *J. Aerosol Sci.*, *29*(10), 1237–1248.

Volten, H., O. Muñoz, E. Rol, J. F. de Haan, W. Vassen, J. W. Hovenier, K. Muinonen, and T. Nousiainen (2001), Scattering matrices of mineral aerosol particles at 441.6 nm and 632.8 nm, *J. Geophys. Res.*, *106*(D15), 17,375–17,402.

von Hoyningen-Huene, W., and P. Posse (1997), Nonsphericity of aerosol particles and their contribution to radiative forcing, *J. Quant. Spectrosc. Radiat. Transfer*, *57*, 651–668.

von Hoyningen-Huene, W., M. Freitag, and J. B. Burrows (2003), Retrieval of aerosol optical thickness over land surfaces from top-of-atmosphere radiance, *J. Geophys. Res.*, *108*(D9), 4260, doi:10.1029/2001JD002018.

von Hoyningen-Huene, W., A. A. Kokhanovsky, J. B. Burrows, V. Bruniquel-Pinel, P. Regner, and F. Baret (2006), Simultaneous determination of aerosol-and surface characteristics from top-of-atmosphere reflectance using MERIS on board of ENVISAT, *Adv. Space Res.*, *37*(12), 2172–2177.

Wang, M., and H. R. Gordon (1994), Radiance reflected from the ocean-atmosphere system: synthesis from individual components of the aerosol size distribution, *Appl. Opt.*, *33*, 7088–7095.

Whitlock, C. H., D. S. Bartlett, and E. A. Gurganus (1982), Sea foam reflectance and influence on optimum wavelength for remote sensing of ocean aerosols, *Geophys. Res. Lett.*, *9*(6), 719–722.

Winker, D. M., J. Pelon, and M. P. McCormick (2003), The CALIPSO mission: Spaceborne lidar for observation of aerosols and clouds, *Proc. SPIE Int. Soc. Opt. Eng.*, *4893*(1), 1–11.

Yang, P., Q. Feng, G. Hong, G. W. Kattawar, W. J. Wiscombe, M. I. Mishchenko, O. Dubovik, I. Laszlo, and I. N. Sokolik (2007), Modeling of the scattering and radiative properties of nonspherical dust-like aerosols, *J. Aerosol Sci.*, *38*(10), 995–1014.

Y. S. Bennouna, Atmospheric Optics Group, University of Valladolid, Prado de la Magdalena, E-47071 Valladolid, Spain. (yasmine@goa.uva.es)

G. de Leeuw, Climate Change Unit, Finnish Meteorological Institute, PO Box 503, Erik Palmenin Aukio 1, FIN-00101 Helsinki, Finland.

J. Kusmierczyk-Michulec, TNO Defence, Security and Safety, Oude Waalsdorperweg, 63 PO Box 96864, NL-2509 JG The Hague, Netherlands.

J. Piazzola, LEPI-LSEET, Université du Sud Toulon-Var, Avenue Georges Pompidou, Batiment X (ISITV), BP 56, F-83162 La Valette du Var, France.